Numerical model for the locomotion of spirilla

M. Ramia
Department of Mechanical Engineering, The University of Sydney, NSW 2006, Australia

ABSTRACT The swimming of trailing, leading, and bipolar spirilla (with realistic flagellar centerline geometries) is considered. A boundary element method is used to predict the instantaneous swimming velocity, counter-rotation angular velocity, and power dissipation of a given organism as functions of time and the geometry of the organism. Based on such velocities, swimming trajectories have been deduced enabling a realistic definition of mean swimming speeds. The power dissipation normalized in terms of the square of the mean swimming speed is considered to be a measure of hydrodynamic efficiency. In addition, kinematic efficiency is defined as the extent of deviation of the swimming motion from that of a previously proposed ideal corkscrew mechanism. The dependence of these efficiencies on the organism's geometry is examined giving estimates of its optimum dimensions. It is concluded that appreciable correlation exists between the two alternative definitions for many of the geometrical parameters considered. Furthermore, the organism having the deduced optimum dimensions closely resembles the real organism as experimentally observed.

1. INTRODUCTION

From a simplified modeling point of view, a microorganism primarily consists of an inert cell body and a helically (or sinusoidally) beating flagellum. As a result of its beating, the flagellum induces a net force and a net moment on the cell body. Hence, the entire organism acquires an instantaneous rigid body swimming velocity $\mathbf{U}$ and angular velocity $\mathbf{\Omega}$ to maintain equilibrium. The locomotion problem is concerned with the prediction of $\mathbf{U}$ and $\mathbf{\Omega}$ for a given geometry of the organism, the wave parameters of the flagellum and the properties of the surrounding fluid.

The classical example has been that of an organism with a spherical (or ellipsoidal) cell body such as the spermatozoa of many mammals, many types of protazoa, and flagellar bacteria. The modeling of such organisms has been approached by a variety of techniques (1–3). The present problem, however, deals with a somewhat different class of microorganisms; namely, those with cell bodies whose centerline curvature is helical. Many bacteria belonging to the order of *Spirochaetales* or the family of *Spirillaceae* fall under this category. *Spirillum volutans* is one such organism and is the subject of the present study.

This organism may possess as many as 75 flagella at either or both ends of its helical body (4). At a given end, the flagella are forced together by the hydrodynamic viscous drag and rotate as a single unit (5). Hence, they are collectively known as a flagellar bundle but will hereafter be simply referred to as a flagellum. As the helical cell body rotates in an opposite sense to that of the flagellum, it spirals its way through the fluid much like a corkscrew driven through a cork (6).

Chwang et al. (6) (hereafter referred to as CWW) modeled the swimming of this organism by replacing the effect of the surrounding fluid with a pair of coefficients representing the respective hydrodynamic resistances to motions normal and tangential to the cell body and flagellar centerlines. This method is known as the Resistive Force Theory (RFT) approach and was first formulated by Gray and Hancock (7). Although it was later refined by Lighthill (8), this approach remains primarily limited to microorganisms which can be modeled by a combination of slender bodies (i.e., bodies possessing small curvature and cross-sectional dimensions as compared with their lengths) and spheroids. Furthermore, it fails to account for hydrodynamic interaction between the cell body and the flagellum. Cinemicrographs of spirilla (4) suggest that their cell bodies are neither slender nor spheroidal, hence the present need for an alternative approach.

Myerscough and Swan (9) (hereafter referred to as MS) considered a distribution of singularities (Stokeslets and Doublets) along the centerlines of the cell body and flagellum (both modeled as cylindrical filaments). By satisfying the no-slip conditions at the boundary (organism's surface) together with the equilibrium conditions, the strengths of the singularities and the velocities $\mathbf{U}$ and $\mathbf{\Omega}$ can be solved for simultaneously. This method, known as the Slender Body Theory (SBT) approach, was first formulated by Hancock (10), and has

0006-3495/91/11/1057/22 $2.00

since been refined by many other workers in the field (11, 2, 12).

Unlike CWW, MS allowed for finite transverse components of $\mathbf{U}$ and $\mathbf{\Omega}$ which are of major significance in modeling the locomotion of spirilla. Hydrodynamic interaction is also accounted for by including the relevant image systems for the respective singularities. Both these models, however, assume the flagellum to be a straight, rigid rod rotating at an angle to the cell body axis, hence, defining a conical surface of revolution. Furthermore, the slender body assumption restricts both models to somewhat unrealistic proportions for the organism.

Winet and Keller (13) carried out experimental observations on the geometry of flagella and investigated its effects on the RFT predictions of $\mathbf{U}$, $\mathbf{\Omega}$, and power dissipation. It was concluded that a rigidly rotating helical flagellum yields the most realistic results. On the other hand, their observations suggested that enough flexibility must exit to allow for the rather high curvature bends near the cell body/flagellar junction. Electron microscopic observations (14) resolved this paradox by revealing the presence of a curved region called the hook (in each flagellar filament), which is attached by a rod to a complex flagellar basal structure.

The kinematics of swimming microorganisms were investigated by Keller and Rubinow (15). They presented an analytical method whereby the swimming paths (trajectories) may be determined for given instantaneous swimming velocities $\mathbf{U}$ and $\mathbf{\Omega}$. This method assumes that both $\mathbf{U}$ and $\mathbf{\Omega}$ are independent of the flagellar phase angle (hence independent of time) and that the radial components of $\mathbf{\Omega}$ are both small compared with its axial component. These are realistic assumptions for the abovementioned case of organisms with spherical cell bodies. Both MS and the present study, however, show that the former of these assumptions does not hold for the case of *S. volutans*.

The present Boundary Element Method (BEM) model is based on the formulation by Tran-Cong and Phan-Thien (16) which, being geometry independent enables the employment of realistic organism geometry and dimensions (such as given by Swan [4]). Based on the observations and calculations of Winet and Keller (13), the geometries of the leading and trailing flagella are refined. A numerical generalization of the method of Keller and Rubinow (15) yields the position of the organism at any instant (i.e., trajectory), thereby allowing for a realistic definition of the mean swimming speed $\overline{U}$. In addition, the organism's orientation at any instant is found giving a qualitative indication of the kinematic efficiency of the swimming motion.

GLOSSARY

a	cell-body radius
a_f	flagellar radius
$\mathbf{A}^{-1}$	a general three-dimensional rotation matrix
$B(B_X, B_Y, B_Z)$	coordinates of the leading cell-body/flagellar joining point (Fig. 1)
BEM	Boundary Element Method
$C(C_X, C_Y, C_Z)$	coordinates of the trailing cell-body/flagellar joining point (Fig. 1)
$\vec{CB}$	displacement vector joining the points B and C
CWW	Chwang, Winet, and Wu (6)
d_1, d_2	temporary parameters used in modeling flagellar geometry (Fig. 2)
D_x, D_y, D_z	respective amplitudes of the sinusoidal variations with time (Fig. 4) of the components of linear velocity, angular velocity, and power
$E(z)$	flagellar amplitude function (Fig. 2)
F, G	joining point and turning point used in modeling the leading flagellar geometry (Fig. 2)
$\mathbf{G}, \mathbf{H}$	known $3N \times 3N$ system matrices resulting from the boundary-integral formulation (20)
h	flag variable distinguishing between points on the cell body and those on a flagellum (Eq. (11)).
H	point of inflection of the amplitude function $E(z)$
$(\hat{\mathbf{k}}_X, \hat{\mathbf{k}}_Y, \hat{\mathbf{k}}_Z)$	instantaneous direction cosines of the z-axis (relative to the globally fixed $[X, Y, Z]$ frame)
k	cell body wavenumber
k_e	parameter determining the rate at which the flagellum grows (with axial distance) to its maximum amplitude
k_f	flagellar wavenumber
l	cell body length
l_f	flagellar length
L	cell body axial extension (Fig. 1)
m	flag variable distinguishing between unipolar and bipolar spirilla (equation (25))
M	point defining the distal end of the flagellum (Fig. 2)
MS	Myerscough and Swan (9)
n	counter variable used for reference to a given boundary element
$\hat{\mathbf{n}}$	unit vector along the axis of propagation
n_c	number of segments used to discretize the cell body centerline
n_f	number of segments used to discretize the flagellar centerline
N	total number of boundary elements used to discretize the entire organism
N_λ	number of cell body wavelengths
P_c, P_f, P_t	instantaneous cell body, flagellar, and total power dissipations, respectively
$\overline{P}_c, \overline{P}_f, \overline{P}_t$	mean cell body, flagellar, and total power dissipations, respectively

$\overline{q}$	mean radial displacement (over the interval $0 \leq t \leq T$) of the trajectories of the points B and C from the axis of propagation (Eq. 22)
q_a	instantaneous axial displacement of the trajectory of the point C (measured along the axis of propagation) (Fig. 6)
q_B	instantaneous radial displacement of the trajectory of the point B (measured from the axis of propagation)
q_C	instantaneous radial displacement of the trajectory of the point C (measured from the axis of propagation)
q_r	as for q_C (Fig. 6)
$r_\perp$	radial component (i.e., normal to the z-axis) of the vector $\mathbf{r}$
$\mathbf{r}$	position vector defining points on the cell body relative to the flagellar (x, y, z) frame (Fig. 5)
$\mathbf{r}^*$	position vector defining points on the cell body relative to the (x^*, y^*, z^*) axes (Fig. 1)
$\mathbf{r}_f$	position vector defining points on the flagellum relative to the flagellar (x, y, z) frame (Fig. 5)
$\mathbf{R}$	position vector defining points on the cell body relative to the globally fixed (X, Y, Z) frame (Fig. 5)
$\mathbf{R}_C$	position of the point C (origin of the $[x, y, z]$ axes) relative to the globally fixed (X, Y, Z) frame (Fig. 5)
$\mathbf{R}_f$	position vector defining points on the flagellum relative to the globally fixed (X, Y, Z) frame (Fig. 5)
RFT	Resistive Force Theory
S_x, S_y, S_z	respective means of the sinusoidal variations with time (Fig. 4) of the components of linear velocity, angular velocity, and power
S_n	surface area of the nth flat triangular boundary element
SBT	Slender Body Theory
t	time
$\mathbf{t}$	traction (local force per unit area)
$\mathbf{t}^{(n)}$	traction on bondary element n
T	period of time (set to 16π) over which the trajectory of the organism is considered namely, the interval $0 \leq t \leq T$
$\mathbf{u}$	vector defining the velocity field on the surface of the organism
u_a	instantaneous axial velocity (along the axis of propagation) of the point C (time derivative of q_a, see Fig. 6)
$\mathbf{u}^{(n)}$	velocity at the centeroid of the nth boundary element
$\mathbf{U}$	instantaneous swimming velocity
$\overline{U}$	mean swimming speed
$\mathbf{U}_l$	Total instantaneous linear velocity of points on a leading flagellum
v_c	number of sides on the polygon used to discretize any given cross-section of the cell body
v_f	number of sides on the polygon used to discretize any given cross-section of flagellum
W	total flagellar angular velocity (relative to the globally fixed $[X, Y, Z]$ frame)
(x, y, z)	axes defining a frame at rest with respect to the flagellum (i.e., flagellar frame)
(x^*, y^*, z^*)	a set of axes defined purely for the purpose of modeling the cell body centerline geometry (Fig. 1)
$\mathbf{x}^{(n)}$	position vector of the centroid of the nth boundary element relative to the point C
(X, Y, Z)	axes defining the globally fixed frame of reference
z_e	axial extension of the flagellum
z_l, z_u	lower and upper limits of integration for calculating the flagellar length (Eq. 9)
α	cell body amplitude (Fig. 1)
α_f	flagellar amplitude, replaced by α_t for trailing and α_l for leading flagella
$\beta_X, \beta_Y, \beta_Z$	direction cosines of the axis of propagation relative to the globally fixed (X, Y, Z) frame
γ	flagellar cone half angle (Fig. 1)
δ	flag variable distinguishing between points lying below and those lying above the turning point G of a leading flagellum
$\Delta\theta$	leading flagellar phase angle relative to the trailing flagellum for a bipolar spirillum
η	fluid viscosity
η_H^{-1}	inverse hydrodynamic efficiency
η_k^{-1}	inverse kinematic efficiency
θ	flagellar phase angle ωt
λ	cell body helical wavelength (Fig. 1)
ρ	instantaneous angle of precession (angle between the cell-body axis and the axis of propagation)
$\overline{\rho}, \rho_m$	mean and maximum angles of precession (over the interval $0 \leq t \leq T$), respectively
ψ_0	a parameter (used in referring points on the cell body to the flagellar frame) related to the initial orientation of the cell body relative to the flagellar frame (Eq. 18)
ϕ_x, ϕ_y, ϕ_z	respective phase lags of the sinusoidal variations with time (Fig. 4) of the components of linear velocity, angular velocity, and power
Ψ, φ, ϑ	Euler angles (as defined in reference 22)
ω	magnitude of the angular velocity of the flagellum relative to the cell body
$\boldsymbol{\omega}$	angular velocity of the flagellum relative to the cell body
$\boldsymbol{\Omega}$	instantaneous angular velocity of the cell body
$\overline{\Omega}$	mean angular velocity of the cell body

2. GEOMETRICAL MODELING

Typically, an old *S. volutans* possesses one flagellar bundle at each end of its somewhat long cell body

(possibly in excess of two wavelengths) and hence is said to be bipolar (see Fig. 1). Generally, both flagella tend to rotate at right angles to the cell body axis (relative to the cell body) with the same angular velocity. As the organism propagates (along the negative z^* direction in Fig. 1) the viscous drag bends both flagella back toward their respective axes of rotation. An approximate representation of the resulting flagellar centerline geometries is illustrated in Fig. 2.

S. volutans multiplies by dividing its cell body to form two cells with shorter cell bodies and a single flagellar bundle. These are said to be unipolar. Depending on the sense of the flagellar rotation, a unipolar cell may assume a leading flagellar position (with the flagellum drawing the cell body behind it) or a trailing position (with the flagellum impelling the cell body in front of it). These are often referred to as leading and trailing spirilla, respectively.

Fig. 1 shows that the organism has a cell body of cross-sectional radius a and length l which is curved to form a helix of axial length L, wavelength λ, and amplitude α. Both the trailing flagellum (of amplitude α_t) and the leading flagellum (of amplitude α_l) are of cross-sectional radius a_f, length l_f, and rotate about their respective axes to define a somewhat conical surface of revolution with a half cone angle γ (see Fig. 2).

The centerline of the cell body, defined by the position vector $\mathbf{r}^*$ is given (referred to the $[x^*, y^*, z^*]$ axes as defined in Fig. 1) by the equation for a left-handed helix;

$$\mathbf{r}^* = (\alpha \sin [kz^*], \alpha \cos [kz^*], z^*), \quad 0 \le z^* \le \lambda N_\lambda, \quad (1)$$

where $k = 2\pi/\lambda$ is the wavenumber and $N_\lambda = L/\lambda$ is the number of wavelengths for the body helix. This, when referred to the (x, y, z) axes (which are parallel and fixed with respect to the $[x^*, y^*, z^*]$ axes and centered at the flagellar joining point C), becomes

$$\mathbf{r} = \left\{2\alpha \cos\left[k\left(\frac{z+2L}{2}\right)\right] \sin\left(\frac{kz}{2}\right), 2\alpha \sin \cdot \left[k\left(\frac{z+2L}{2}\right)\right] \sin\left(\frac{-kz}{2}\right), z\right\}, \quad -L \le z \le 0. \quad (2)$$

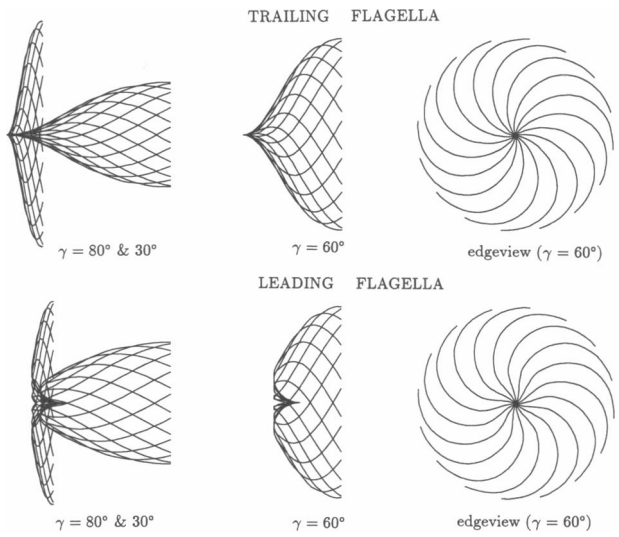

FIGURE 2 Position of flagellar centerlines at 16 distinct phase angles θ for various cone angles γ.

The position vector $\mathbf{r}_f$ defining the flagellar centerline may (referred to the $[x, y, z]$ axes) be expressed in the form

$$\mathbf{r}_f = [\alpha_f E(z) \cos (k_f z + \theta), \alpha_f E(z) \sin (k_f z + \theta), z], \quad 0 \le z \le z_e, \quad (3)$$

where α_f (i.e., α_t or α_l), θ, and k_f are the amplitude, phase angle and wavenumber of the (right handed) flagellar helix. $E(z)$ is an amplitude modifying function (as shown in Fig. 3) which is described by the line $C\ H\ M$, for the trailing flagellar case, and the line $F\ G\ H\ M$, for the leading flagellar case.

For the line $C\ H\ M$, the amplitude function

$$E(z) = 1 - \exp [-(k_e z)^2], \quad (4)$$

of Higdon (17) has been adopted, where k_e is a constant determining the rate at which $E(z)$ grows asymptotically

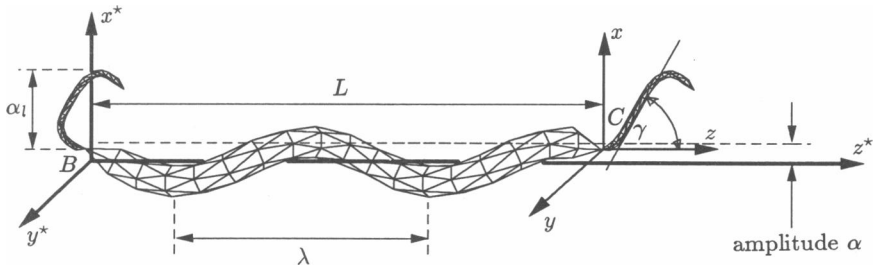

FIGURE 1 Definition of axes and geometrical parameters.

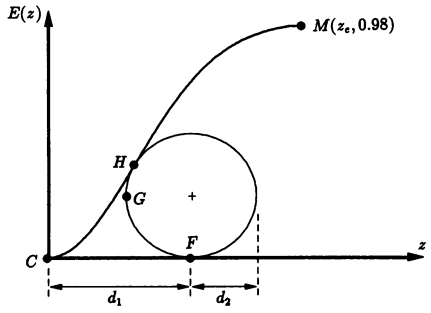

FIGURE 3 Functions defining the leading and trailing flagellar amplitude envelopes.

to its maximum value of 1. It is found that an appropriate choice for k_e and z_e gives rise to an amplitude envelope which realistically models the trailing flagellar geometry. Allowing the amplitude function to grow to 0.98 and equating γ to the slope $E'(z)$ at the point of inflection $H(1/k_e\sqrt{2}, 1 - e^{-1/2})$ gives rise to the respective constraints

$$z_e = \frac{2}{k_e}, \quad k_e\sqrt{2}e^{-1/2} = \tan\gamma, \tag{5}$$

which for a given value of γ uniquely specify k_e and z_e.

There remain the helical wave parameters α_f and k_f to be specified subject to having a constant number of flagellar wavelengths for all given half cone angles γ. It is found that assuming $\alpha_f k_f = \tan\gamma$ (which allows for ~ 0.27 wavelengths) yields the most acceptable qualitative agreement between flagellar geometries as given by Eq. 3 (Fig. 2) and experimental observations (see, for example, Fig. 5 of Winet and Keller [13]). Because $\alpha_f = 1$ is taken to be the fundamental common dimension for all organism discretizations, γ is the only remaining wave parameter for the trailing flagellum $C\,H\,M$.

For the leading flagellar case, the portion $C\,H$ is replaced by a circular arc $F\,G\,H$ of radius d_2 and center (d_1, d_2). Here, Eq. 4 is replaced by

$$E(z) = d_2 + \delta\sqrt{d_2^2 - (z - d_1)^2}, \quad \begin{cases}\delta = -1 \text{ for points on } FG,\\ \delta = 1 \text{ for points on } GH.\end{cases} \tag{6}$$

Imposing continuity of $E(z)$ and $E'(z)$ at H gives

$$\left(d_1 - \frac{1}{k_e\sqrt{2}}\right)^2 = (1 - e^{-1/2})^2 - 2d_2(1 - e^{-1/2}),$$

$$d_2^2 = \left(d_1 - \frac{1}{k_e\sqrt{2}}\right)^2\left(\frac{e}{2k_e^2} + 1\right) \tag{7}$$

which, upon solving simultaneously and selecting the appropriate roots, gives d_1 and d_2 as

$$d_1 = \frac{1}{k_e\sqrt{2}} + d_2\sqrt{\frac{2k_e^2}{e + 2k_e^2}},$$

$$d_2 = \left(\frac{e + 2k_e^2}{2k_e^2}\right)(1 - e^{-1/2})\left(1 - \sqrt{1 - \frac{2k_e^2}{e + 2k_e^2}}\right). \tag{8}$$

The flagellar length l_f is given in general form by the integral

$$l_f = \int_{z_l}^{z_u}\sqrt{1 + [\alpha_f k_f E(z)]^2 + [\alpha_f E'(z)]^2}\,dz \tag{9}$$

which, given suitable choices for $E(z)$ and the limits z_l and z_u, can be solved numerically to obtain the trailing and leading flagellar lengths. For the case of bipolar spirilla, an iterative procedure is set up whereby the amplitude of the leading flagellum α_l is determined by equating both flagellar lengths (with all other parameters maintained constant).

The instantaneous swimming velocity **U**, instantaneous angular velocity $\boldsymbol{\Omega}$, and instantaneous power dissipations (and consequently the means of these quantities) of an organism are functions of the its geometry. For unipolar trailing and leading spirilla, this geometry at a given instant is fully specified via the nine parameters: α, k, N_λ, γ, l_f, l, a_f, a (as defined in Fig. 1) and the flagellar phase angle θ relative to the cell body. For bipolar spirilla, the phase angle of the leading flagellum relative to the trailing flagellum $\Delta\theta$ also needs to be specified. Based on the similar models of Higdon (17) and MS, these are expressed as seven dimensionless parameters: αk, N_λ, γ, (l_f/l), (a/l), (a_f/a), and θ.

The flagellar amplitude α_f is assigned a value of 1 throughout and the flagellar cone angle γ is specified which from Eq. 5 give k_e and z_e. Eqs. 4, 6, and 8 then define the flagellar amplitude functions $E(z)$ and the flagellar length l_f is calculated from Eq. 9. Next, (l_f/l) is specified giving the cell body length l and the parameters k, N_λ, and θ are specified. The axial extension L is calculated as $l/\sqrt{1 + (\alpha k)^2}$ and Eqs. 2 and 3 then define the cell body and flagellar centerlines. Finally, the cell body and flagellar radii are specified via the parameters (a/l) and (a_f/a). The equations defining the cell body and flagellar surfaces may be given in terms of their respective centerline geometries, and radii a and a_f(3). The present discretisation scheme, which is based on these equations, is outlined briefly in Appendix 1 but is discussed at length by Ramia and Phan-Thien (18).

From cinemicrographs (Fig. 3 in Swan [4]) typical values of the geometrical parameters of the organism were estimated. These are summarized in Table 1. Unless otherwise specified, all parameters are maintained constant at their default values as given in this

TABLE 1 **Typical dimensions of modeled cells**

Parameter	Description	Default value
αk	Dimensionless body helix wavenumber	0.500
N_λ	Number of wavelengths in body helix	1.200
γ	Flagellar cone half angle	60.0°
(l_f/l)	Flagellar length to body length ratio	0.500
(a/l)	Body radius to body length ratio	0.045
(a_t/a)	Flagellar radius to body radius ratio	0.200

Unless otherwise specified, all dimensions are as given in this table.

table. The range through which these parameters were varied was determined with the aid of existing models (CWW and MS). The organism geometries representative of either extreme of the considered range are shown in parts *d* and *e* of Figs. 7–14.

3. BOUNDARY ELEMENT METHOD

It is generally accepted that the fluid mechanics associated with the swimming of microorganisms is governed by the Stokes equations (3). Here, the fluid is assumed to be Newtonian, incompressible, inertialess, and highly viscous. The boundary-integral formulation for this so-called Stokes flow problem has been well documented (19, 20) and will not be discussed here. For a body discretized into N constant boundary elements, the boundary traction vector $\mathbf{t}$ (i.e., the force acting on a given element divided by the surface area of that element) may be related to the velocity boundary conditions $\mathbf{u}$ via the expression (20)

$$\mathbf{Hu} = \mathbf{Gt}. \tag{10}$$

Where, $\mathbf{H}$ and $\mathbf{G}$ are known $3N \times 3N$ matrices depending only on the geometry of the boundary. Here, the velocity and traction vectors (each of dimension $3N$) are arranged such that u_1, u_2, u_3 are the vector components of the constant velocity $\mathbf{u}^{(1)}$ at element 1, t_1, t_2, t_3 are the vector components of the constant traction $\mathbf{t}^{(1)}$ at element 1, u_4, u_5, u_6 are the vector components of the constant velocity $\mathbf{u}^{(2)}$ at element 2, etc.

Under steady-state swimming conditions, the velocity field at the boundary is given by (3)

$$\mathbf{u}^{(n)} = \mathbf{U} + (\boldsymbol{\Omega} + h\boldsymbol{\omega}) \times \mathbf{x}^{(n)}, \qquad \begin{cases} h = 0 \text{ for elements on the cell body,} \\ h = 1 \text{ for elements on the flagellum,} \end{cases} \tag{11}$$

where $\mathbf{U}$ is the total linear velocity of the cell body/flagellar joining point C, $\boldsymbol{\Omega}$ is the angular velocity of the cell body about this point, and $\mathbf{u}^{(n)}$ is the velocity at the centroid of element n whose position is denoted by $\mathbf{x}^{(n)}$. In all cases (i.e., for leading, trailing, and bipolar spirilla) $\mathbf{x}^{(n)}$ is taken relative to the (x, y, z) axes (as defined in Fig. 1). For bipolar spirilla this is made possible by replacing $\mathbf{U}$ with $\mathbf{U}_1 = \mathbf{U} + (\overrightarrow{CB} \times \boldsymbol{\Omega})$(where $\overrightarrow{CB}$ represents the displacement vector joining the points C and B) for elements on the leading flagellum. Here, $\boldsymbol{\omega}$ is the known angular velocity of the flagellum relative to the cell body about the z-axis (i.e., $\boldsymbol{\omega} = [0, 0, \omega]$). Due to the Newtonian (i.e., linear) nature of the fluid, tractions (and consequently forces, moments, swimming velocities, etc.) are directly proportional to ω and the fluid viscosity η. Hence they are each assigned a value of 1 for all calculations and are used as normalizing factors.

Equilibrium requires that the net force and moment on the organism must vanish. Thus,

$$\sum_{n=1}^{N} S_n \mathbf{t}^{(n)} = 0, \quad \sum_{n=1}^{N} S_n \mathbf{t}\mathbf{x}^{(n)} \times \mathbf{t}^{(n)} = 0 \tag{12}$$

where S_n is the area of element n and $\mathbf{t}^{(n)}$ is the traction vector of this element. Substitution for the tractions (from Eq. 10) and velocities (from Eq. 11) in Eq. 12 results in six scalar equations for which the six unknown components of $\mathbf{U}$ and $\boldsymbol{\Omega}$ can be solved. An alternative method whereby $\mathbf{U}$ and $\boldsymbol{\Omega}$ may be determined from Eq. 10 and the associated equilibrium conditions has also been considered by Ramia and Tullock (21).

The total instantaneous power P_t dissipated by the organism in swimming is given by

$$P_t = \sum_{n=1}^{N} S_n \mathbf{t}^{(n)} \cdot \mathbf{u}^{(n)}. \tag{13}$$

The power dissipated by the cell body P_c or by the flagellum P_f may also be calculated by replacing the summation limits in Eq. 13 with the appropriate element ranges. The typical errors (in $\mathbf{U}$, $\boldsymbol{\Omega}$, and P_t as predicted by Eqs. 10–13) introduced by discretizing the organism's outer surface into N boundary elements are discussed in Appendix 1.

The instantaneous linear velocity $\mathbf{U}$ has been considered, by CWW and MS, in normalized form as $k\mathbf{U}/\omega$, where $k = 2\pi/\lambda$ is the wavenumber of the cell body helix. Similarly, the angular velocity $\boldsymbol{\Omega}$ is normalized as $\boldsymbol{\Omega}/\omega$. Fig. 4 shows the present Boundary Element predictions of these normalized quantities at 16 values of the flagellar phase angle θ for a unipolar trailing cell with the typical dimensions of Table 1.

It is immediately apparent that, for this organism of typical dimensions and geometry, the radial components of linear velocity and angular velocity vary appreciably with the flagellar phase angle through a given cycle. A

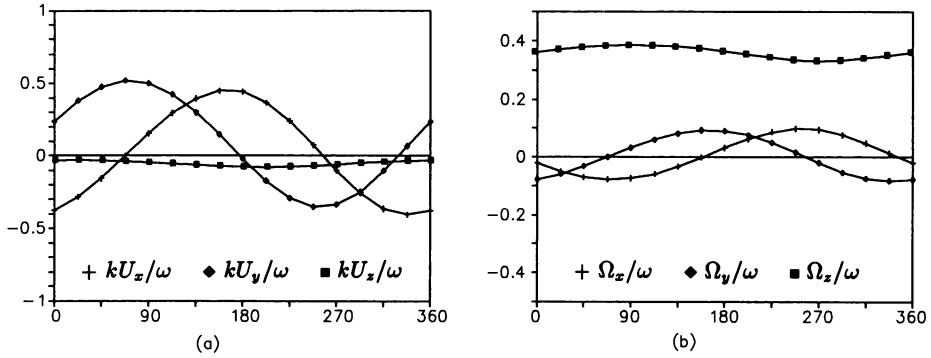

FIGURE 4 Graphs of normalized (*a*) linear and (*b*) angular velocity components $k\mathbf{U}/\omega$ and $\Omega/\mathbf{\Omega}$, respectively, vs. flagellar phase angle θ (deg).

similar trend is also observed for the normalized power which, for the purposes of the present section, is given as $kP/\eta(\alpha\omega)^2$. This could only be due to the dependence of the cell body/flagellar hydrodynamic interaction on the flagellar orientation and is a direct consequence of the asymmetry of the cell body. At a given instant in the cycle, the major part of the flagellum could be at its furthest distance from the cell body, at which point this interaction would be minimal whilst at some other instant in the cycle the opposite situation may exist. These variations were not exhibited by the RFT model of CWW because their approach inherently neglects such hydrodynamic interactions.

The variations of linear velocity, angular velocity, and power with time may be modeled by a sinusoidal function of mean S, amplitude D, and phase lag ϕ. This could take the form $S_x + D_x \sin(\omega t - \phi_x)$ (for the x component of linear velocity, for example) with ωt replacing θ and t representing time. It is found that a least squares fit of this function with the points of Fig. 4 approximates these variations, typically to within 0.5%.

In Table 2, the values of the parameters S, D, and ϕ resulting from the consideration of eight instants per flagellar cycle are compared with those of 16 instants. The largest errors are 7.37% and 9.84%, for the parameter ϕ_z. These errors may be considered tolerable because they both relate to waveforms whose amplitudes are small compared with their means. The only remaining appreciable error is that of 2.01% for the normalized sinusoidal mean of Ω_y. This may also be overlooked as it reduces to 0.08% when the magnitude (which is of primary interest here) of the angular velocity vector is considered. It is then concluded that the use of eight instants (per flagellar cycle) may safely be adopted for all subsequent calculations as it yields sufficient accuracy in modeling the variation of velocity, angular velocity, and power with flagellar phase angle (or time).

4. KINEMATICS

Let $\mathbf{r}_f(t)$ represent any position vector in the flagellar fixed (x, y, z) frame (i.e., fixed with respect to the flagellum and will hereafter be referred to as the flagellar frame), and $\mathbf{R}_f(t)$ be this vector referred to the globally fixed (X, Y, Z) frame (see Fig. 5) at a given time t. The tranformation from $\mathbf{r}_f(t)$ to $\mathbf{R}_f(t)$ consists of a translation by $\mathbf{R}_c(t)$ and a rotation by $\mathbf{A}^{-1}(t)$ (15):

$$\mathbf{R}_f[\mathbf{r}_f(t), t] = \mathbf{R}_C(t) + \mathbf{A}^{-1}(t)\mathbf{r}_f(t),$$
$$\frac{d\mathbf{R}_C(t)}{dt} = \mathbf{A}^{-1}(t)\mathbf{U}(t), \tag{14}$$

where $\mathbf{U}(t)$ is the linear velocity of the flagellar frame defined by the instantaneous swimming velocity (such as that depicted in Fig. 4 *a* whose components vary sinusoidally with time) and $\mathbf{A}^{-1}(t)$ is a 3×3 rotation matrix which may be expressed in terms of the Euler angles $\varphi(t)$, $\vartheta(t)$, and $\Psi(t)$ (Eq. 4–47 of Goldstein [22]) as

$$\mathbf{A}^{-1} = \begin{pmatrix} \cos\Psi\cos\varphi - \cos\vartheta\sin\varphi\sin\Psi & -\sin\Psi\cos\varphi - \cos\vartheta\sin\varphi\cos\Psi & \sin\vartheta\sin\varphi \\ \cos\Psi\sin\varphi + \cos\vartheta\cos\varphi\sin\Psi & -\sin\Psi\sin\varphi - \cos\vartheta\cos\varphi\cos\Psi & -\sin\vartheta\cos\varphi \\ \sin\vartheta\sin\Psi & \sin\vartheta\cos\Psi & \cos\vartheta \end{pmatrix}. \tag{15}$$

Furthermore, these angles are in turn related to the absolute angular velocity of the flagellar frame $\mathbf{W}$ via the expression (eq. 4–47 of Goldstein [22])

$$\mathbf{W} = (\dot{\varphi}\sin\vartheta\sin\Psi + \dot{\vartheta}\cos\Psi, \dot{\varphi}\sin\vartheta\cos\Psi - \dot{\vartheta}\sin\Psi, \dot{\varphi}\cos\vartheta + \dot{\Psi}). \tag{16}$$

Rearranging, and replacing $\mathbf{W}$ with $\mathbf{\Omega} + \boldsymbol{\omega}$ results in the

TABLE 2 **Calculated mean, amplitude, and phase lags for the sinusoidal functions approximating the variation of velocity, angular velocity, and power dissipation with time (for a unipolar trailing Spirillum with the dimensions of Table 1)**

Quantity	Calculated values (8 points) $\frac{kU}{\omega}$	$\frac{\Omega}{\omega}$	$\frac{kP}{\eta(\alpha_f\omega)^2}$	% errors $\frac{kU}{\omega}$	$\frac{\Omega}{\omega}$	$\frac{kP}{\eta(\alpha_f\omega)^2}$
			Sinusoidal mean			
S_x	0.03116	0.0077	0.7870	1.31	0.74	0.59
S_y	0.09716	0.0063	1.0969	0.67	2.01	0.46
S_z	−0.05315	0.3615	1.8839	0.71	0.08	0.53
			Sinusoidal amplitude			
D_x	0.4263	0.08819	0.1202	0.33	0.20	0.50
D_y	0.4353	0.08761	0.2476	0.07	0.82	0.20
D_z	0.0238	0.02643	0.3682	0.95	0.75	0.24
			Sinusoidal phase lag			
ϕ_x	76.0	164.0	195.0	0.00	0.00	0.97
ϕ_y	180.0	76.0	194.0	0.00	0.00	0.51
ϕ_z	−76.0	50.0	195.0	7.37	9.84	1.02
			Magnitude $S = (S_x^2 + S_y^2 + S_z^2)^{1/2}$			
S	0.1150	0.3616	—	0.70	0.08	—

Note, the power components are those of the cell body, flagellar, and total power dissipations, respectively.

set of first order ordinary differential equations

$$\begin{pmatrix} \dot{\varphi} \\ \dot{\vartheta} \\ \dot{\Psi} \end{pmatrix} = \begin{pmatrix} \sin\Psi/\sin\vartheta & -\cos\Psi/\sin\vartheta & 0 \\ \cos\Psi & -\sin\Psi & 0 \\ -\cot\vartheta\sin\Psi & -\cot\vartheta\sin\Psi & 1 \end{pmatrix} \begin{pmatrix} \Omega_x \\ \Omega_y \\ \Omega_z + \omega \end{pmatrix}, \quad (17)$$

where $\boldsymbol{\Omega}$ is typically a sinusoidal function of time (see Fig. 4 for example).

The numerical solution of these equations, with appropriate initial conditions (presently a fourth order Runge-Kutter scheme is employed to yield a solution which has converged to within 0.5%) for the Euler angles specifies the rotation matrix of Eq. 15 giving the trajectory of the point C and any point in the flagellar frame R_f from Eqs. 14.

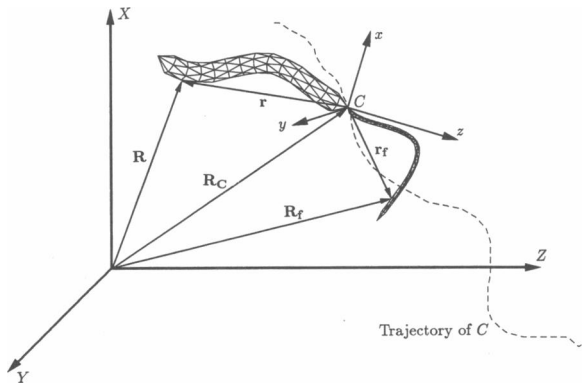

FIGURE 5 Definition of the variables and axes associated with the modeling of swimming kinematics.

Any position vector $\mathbf{r}$ in the body frame (i.e., a frame at rest with respect to the cell body) rotates with an angular velocity $-\boldsymbol{\omega} = (0, 0, -\omega)$ relative to the flagellar frame. When referred to the flagellar frame such a vector is given by

$$\mathbf{r}_f = [r_\perp \cos(\psi_o - \omega t), r_\perp \sin[\psi_o - \omega t], r_z),$$
$$\psi_o = \tan^{-1}\left(\frac{r_y[0]}{r_x[0]}\right), \quad (18)$$

where $r_x(0)$ and $r_y(0)$ are the initial values of the x and y components of $\mathbf{r}$ at $t = 0$, respectively, and $r_\perp = \sqrt{r_x^2 + r_y^2}$ is its radial component (i.e., the component normal to the z-axis). This may in turn be referred to the globally fixed frame via the first of Eqs. 14 giving the trajectory of any point in the body frame, and specifically, of any point on the cell body surface.

Although Keller and Rubinow (15) considered the kinematics of the simpler axisymmetric cell bodied organism, their results bear qualitative relevance to the present study. In particular, the trajectory of the point C describes a helix about the axis of propagation (namely the Z-axis). Furthermore, the z-axis defines a constant angle with the Z-axis and precesses about it with a constant angular velocity depicting (in a frame at rest with respect to the point C) a cone of precession (i.e., a conical surface of revolution). Hence, without prior knowledge of the angle of precession, it is not possible to select a suitable set of initial conditions to ensure that the direction of propagation lies along the Z-axis.

It is necessary to assign a nonzero initial value to the Euler angle ϑ because the x and z components of Eqs. 17 are both singular at $\vartheta = 0$. Presently, for the parameters considered in Eqs. 17 the solution for $\vartheta(t)$ as a function of time rarely varies by more than 20° (which is evident by the results of Figs. 7–14). Hence, the initial value $\vartheta(0) = 90°$ ensures that this angle does not venture to the vicinity of 0°. The initial conditions associated with the remaining Euler angles, however, are not subject to any such constraint and are both set to zero. Thus, $\varphi(0) = \Psi(0) = (0)$ and $\vartheta(0) = 90°$.

The unit vector along the axis of propagation $\hat{\mathbf{n}} = (\beta_X, \beta_Y, \beta_Z)$ (referred to the fixed frame) is given by

$$\hat{\mathbf{n}} = \frac{1}{T}\int_0^T (\hat{\mathbf{k}}_X, \hat{\mathbf{k}}_Y, \hat{\mathbf{k}}_Z)dt, \quad (19)$$

where $(\hat{\mathbf{k}}_X, \hat{\mathbf{k}}_Y, \hat{\mathbf{k}}_Z)$ represent the instantaneous direction cosines of the z-axis and are given by the respective elements of the third column in the transformation matrix $\mathbf{A}^{-1}$. The upper limit of integration T represents a time duration which must be significantly larger than

and an exact multiple of the flagellar period 2π (here, $T = 16\pi$ for all calculations). All such axes of propagation together with their associated trajectories and cones of precession are successively rotated through the angle $(-\cos^{-1}\beta_Z)$ about the Z-axis and then through $[\pi - \tan^{-1}(\beta_Y/\beta_X)]$ about the Y-axis, such that the resulting swimming direction is consistently aligned with the negative Z-axis. This has the effect of simplifying the resolution of displacements into two components, namely those parallel to the axis of propagation and those perpendicular to it (as considered in Fig. 6).

Close examination of the many trajectories for organisms of various geometries (such as in Figs. 6, *a* and *b*), reveals that they may generally be rationalized via minor refinements of the results of Keller and Rubinow (15). Both the angle of precession ρ and the helical amplitude q_r of the trajectory of C vary periodically with each flagellar cycle (see Fig. 6 *c* where these are plotted in normalized form as functions of the normalized axial displacement q_a/α_f). Geometrically, the cylinder defining the helical trajectory is replaced by the annular volume of two coaxial cylinders within which the point C is confined to move. Similarly (in a frame at rest with respect to the point C), the z-axis is confined to move within a conical shell of diminishing thickness as its apex.

The time variation of the axial velocity u_a describes a waveform whose period equals that of the flagellar period (see Fig. 6 *d* where both the normalized axial displacement and velocity are plotted as functions of time). Hence, the mean of this waveform for an integral number of flagellar cycles (here 8) represents the kinematically defined mean swimming speed $\overline{U}$ for the organism in question. For the mean angular velocity $\overline{\Omega}$, however, the sinusoidal mean definition of Table 2 is sufficient since its radial x and y components are both small compared with the axial z component (see Fig. 4 *b*).

5. RESULTS

The abovementioned mean swimming speed $\overline{U}$ and mean angular velocity $\overline{\Omega}$ are normalized to $k\overline{U}/\omega$ and $\overline{\Omega}/\omega$, respectively. These are shown as functions of the dimensionless geometrical parameters (defined in Table 1) in parts *a* of Figs. 7–14.

Higdon (17) normalized the total power dissipation $\overline{P}_t$ with respect to the power consumed in rigidly translating the cell body with a velocity $\overline{U}$ (this is given by $6\pi\eta a\overline{U}^2$ where a is the radius of the assumed spherical cell body). He argued that the resulting ratio $\overline{P}_t/6\pi\eta a\overline{U}^2$ may be used as a reciprocal measure of hydrodynamic efficiency as its minimum corresponds to the minimum power dissipated for a given square of the swimming speed.

Although an exact analytic expression for the power

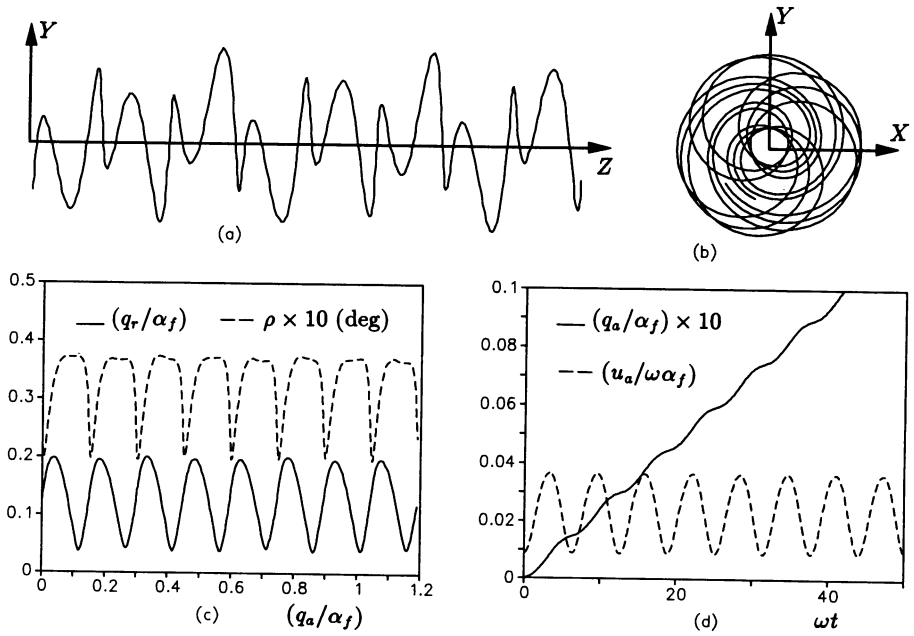

FIGURE 6 (*a*) Sideview and (*b*) edgeview of the trajectory of the joining point C. (*c*) Graph of normalized radial displacement q_r/α_f of the point C and angle of precession ρ (deg) vs. normalized axial displacement q_a/α_f. (*d*) Graph of normalized axial displacement q_a/α_f and normalized axial velocity $u_a/\omega\alpha_f$ vs. dimensionless time ωt (each representing eight flagellar cycles).

needed to rigidly translate the helical cell body of a spirillum is not possible, it is known that this power will be proportional to $\overline{U}^2$. Hence an inverse hydrodynamic efficiency (which was also employed by MS) may be defined as

$$\eta_H^{-1} = k\overline{P}_t/\eta\overline{U}^2. \tag{20}$$

This together with the normalized cell body and flagellar power dissipations ($k\overline{P}_c/\eta\overline{U}^2$ and $k\overline{P}_f/\eta\overline{U}^2$, respectively) are plotted as functions of the geometrical parameters in parts *b* of Figs. 7–14.

The trajectories of the points $B(B_X, B_Y, B_Z)$ and $C(C_X, C_Y, C_Z)$ are determined within the domain $0 \leq t \leq T$ (where $T = 16\pi$) for each of the organism geometries considered. The radial displacements q_B and q_C of these points from the axis of propagation are given by

$$q_B = \sqrt{B_X^2 + B_Y^2} \quad \text{and} \quad q_C = \sqrt{C_X^2 + C_Y^2}. \tag{21}$$

A radial displacement $\overline{q}$ is defined to be the mean of the quantity $(q_B + q_C)/2$ within the domain considered, hence

$$\overline{q} = \frac{1}{T}\int_0^T \left(\frac{q_B + q_C}{2}\right) dt. \tag{22}$$

Similarly, a mean angle of precession $\overline{\rho}$ is defined by

$$\overline{\rho} = \frac{1}{T}\int_0^T \rho(t)\, dt. \tag{23}$$

For the proposed ideal corkscrew motion (6) the mean swimming speed $\overline{U}$ is given identically by the magnitude of the constant instantaneous linear velocity **U** which presumably has zero radial components. In addition, this swimming speed must match the constant cell body helical wave speed $\overline{\Omega}/k$ such that the cell body is propelled through the fluid without any "apparent wave slippage" (23). Based on this mechanism alone, every part of the cell body would always be moving in a direction tangential to its helical centerline. The hydrodynamic resistance to this type of tangential motion is approximately between 0.5 and 0.7 times smaller than the resistance to normal motions (6). Such normal motions are introduced by the nonzero radial components of linear and angular velocity and are reflected by the deviation from the conditions $(\overline{q}/\alpha) = 1$ and $\overline{\rho} = 0$. Hence,

$$\eta_k^{-1} = \left|1 - \left(\frac{\overline{q}}{\alpha}\right)\right| \tag{24}$$

may be considered to be an inverse kinematic efficiency because the extent of its deviation from the minimum value of zero is indicative of the digression from the ideal corkscrew swimming motion. A similar interpretation follows for the normalized mean precession angle $\overline{\rho}/\alpha$ which along with η_k^{-1} are shown as functions of the geometrical parameters in parts *c* of Figs. 7–14.

Consider the point $\mathbf{r}_f = (0, 0, 1)$ on the *z*-axis in the flagellar frame and let $\mathbf{R}_C = 0$ (for all *t*) whereby Eqs. 14 give the trajectory of this point in a frame rotating but not translating with the flagellar frame. The maximum radial displacement of any point on this trajectory defines the sine of the maximum angle of precession ρ_m. A cone having an axis aligned with the *Z* direction and an apex angle of $2\rho_m$ is referred to as the the cone of precession. In addition, a cylinder whose surface contains the cell body helical centerline is considered to be the body cylinder (see Fig. 8 *d*). Typical trajectories of *B* and *C*, superimposed on the associated body cylinders and cones of precession are shown in parts *f* and *g* of Figs. 7–14.

5.1. Unipolar trailing spirilla

Fig. 7 shows the results relating to variations in the number of cell body wavelengths N_λ. For very small values of this parameter (~ 0.1) the cell body is nearly axisymmetric and offers minimal resistance to rotation. As N_λ increases, however (to ~ 1), the cell body tends to deviate slightly from this condition leading to a decrease in $\overline{\Omega}/\omega$. Here, the exceedingly large precession angles are due to the insufficient number of cell body wavelengths rendering the corkscrew mechanism ineffective (see Fig. 7 *f*). This together with the increase in the normalizing factor *k* give rise to the initial inverse relationship between $k\overline{U}/\omega$ and $\overline{\Omega}/\omega$. Beyond this point, the associated decrease in cell body amplitude (compare Fig. 7 *d* to Fig. 7 *e*) reduces its resistance to rotation, and an approach of the direction of this rotation to that of the cell body axis (compare Fig. 7 *f* to Fig. 7 *g*). Hence, the slow but consistent increase in $\overline{\Omega}/\omega$. The relatively small values of $\overline{\rho}$ (for $N_\lambda > 1$) are further evidence of the effectiveness of the corkscrew mechanism whereby $k\overline{U}/\omega$ increases directly with $\overline{\Omega}/\omega$.

The graph showing the inverse hydrodynamic efficiency in Fig. 7 *b* exhibits no optimum with the organisms having fewer cell body wavelengths (i.e., N_λ small) being more hydrodynamically efficient. On the other hand, $\overline{\rho}$ is acceptably small for $N_\lambda > 1$ whilst experimental observations lie predominantly in the range $2 \geq N_\lambda \geq 1$.

The inverse kinematic efficiency η_k^{-1} oscillates wildly between low and high values as the number of cell body wavelengths N_λ varies through the given range (hence the lack of smoothness in the graphs of $k\overline{U}/\omega$,$\overline{\Omega}/\omega$ and power dissipation components shown in Figs. 7 *a* and *b*. This is almost certainly due to the relative angular positions of the points *B* and *C* when viewed along the cell body axis. For an exact number of cell body wave-

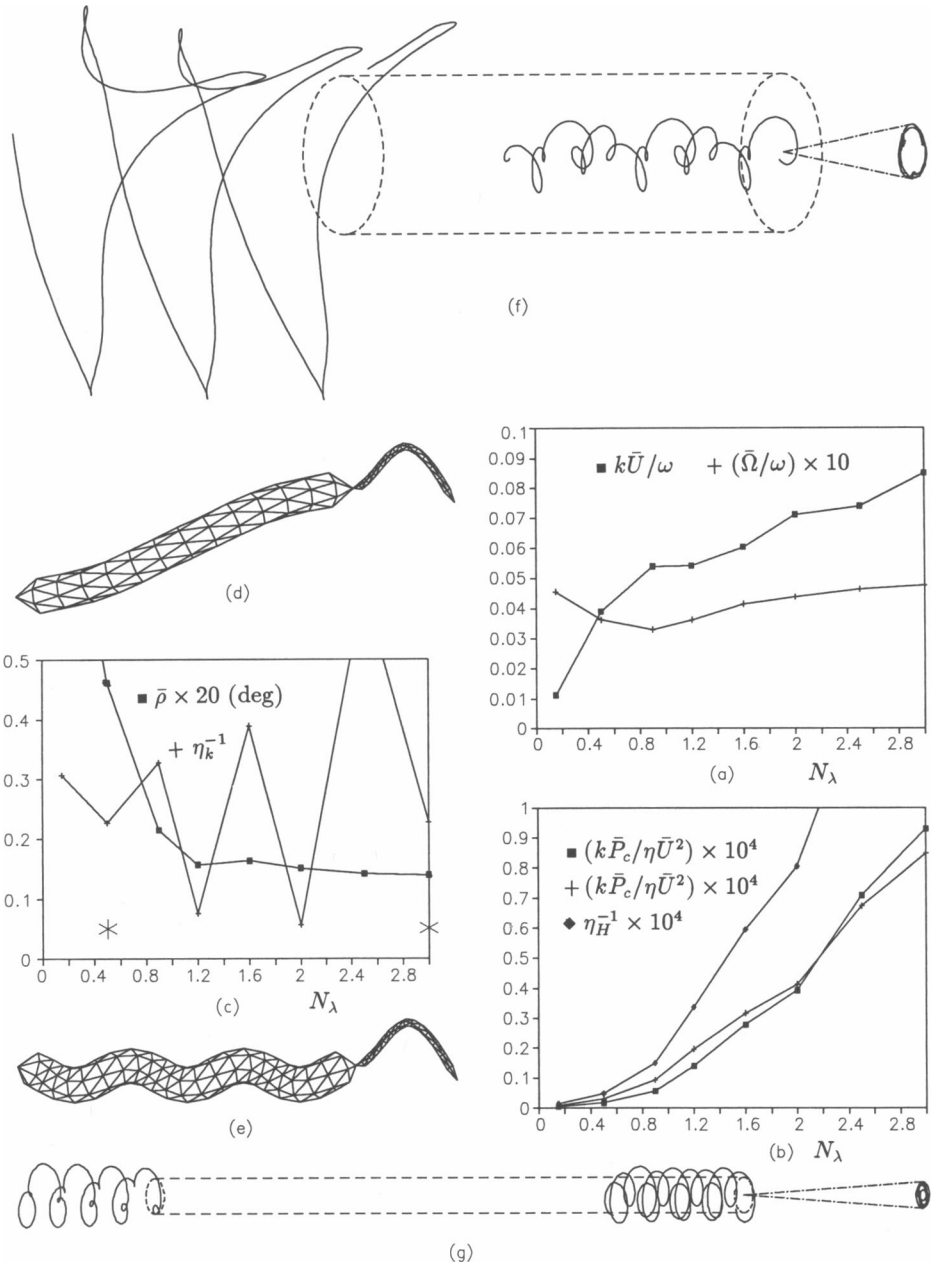

FIGURE 7 (*a*) Graph of normalized mean swimming speed $k\overline{U}/\omega$ and normalized mean angular velocity $\overline{\Omega}/\omega$ vs. the number of cell-body wavelengths N_λ for unipolar trailing spirilla. (*b*) Graph of normalized mean power dissipation components $k\overline{P}/\eta\overline{U}^2$ (with $\overline{P}$ representing the cell-body power $\overline{P}_c$, the flagellar power $\overline{P}_f$, or the total power dissipation $\overline{P}_t$) vs. the number of cell-body wavelengths N_λ. (*c*) Graph of inverse kinematic efficiency η_k^{-1} and the mean angle of precession $\bar{\rho}$ vs. the number of cell-body wavelengths N_λ. (*d and e*) Boundary element meshes for organisms with parameter values $N_\lambda = 0.5$ and $N_\lambda = 3$ (shown as * on the graph of part *c*), respectively. (*f and g*) trajectories (representing eight flagellar cycles) of the leading point *B* and joining point *C* superimposed on the body cylinder and cone of precession (viewed at 30° to the plane of the page) for the organisms shown in *d* and *e*, respectively.

lengths, *B* and *C* coincide (in this view) and any slight rigid-body rotation of the cell body axis relative to the *Z*-axis is in one case additive to and the other subtractive from the quantity $(q_B + q_C)/2$. This is not the case for fractional number of wavelengths and in particular for half wavelengths (i.e., ½, 1½, 2½ . . .), where these points are at opposite ends of the body cylinder's cross-section. Hence, it appears that these two cases define the respective lower and upper bounds on $\bar{q}$ and consequently on η_k^{-1}.

Fig. 8 shows the results relating to variations in the normalized cell body radius a/l. As this parameter increases (other parameters remaining constant) both the cell body and flagellar radii increase proportionately whilst their centerline geometries remain unaltered (compare Fig. 8 *d–e*). Here, the flagellar torque increases with the flagellar radius, but this effect is grossly overshadowed by the quicker increase of the cell-body rotational inertia with the cell-body radius. Hence, $\overline{\Omega}/\omega$ and consequently $k\overline{U}/\omega$ (as a result of the corkscrew mechanism) decrease with a/l. The opposite is the case for the inverse hydrodynamic efficiency (Fig. 8 *b*) where more power is dissipated in rotating and propelling the thicker cell bodies and flagella. Both these trends are in agreement with the results of CWW where it is reported that organisms with thin cell bodies swim more efficiently than those with thicker cell bodies. The inverse kinematic efficiency and the mean precession angle vary negligibly with a/l throughout the considered range reflecting the fact that the kinematics depend primarily on the centerline geometries.

Fig. 9 shows the results relating to variations in the

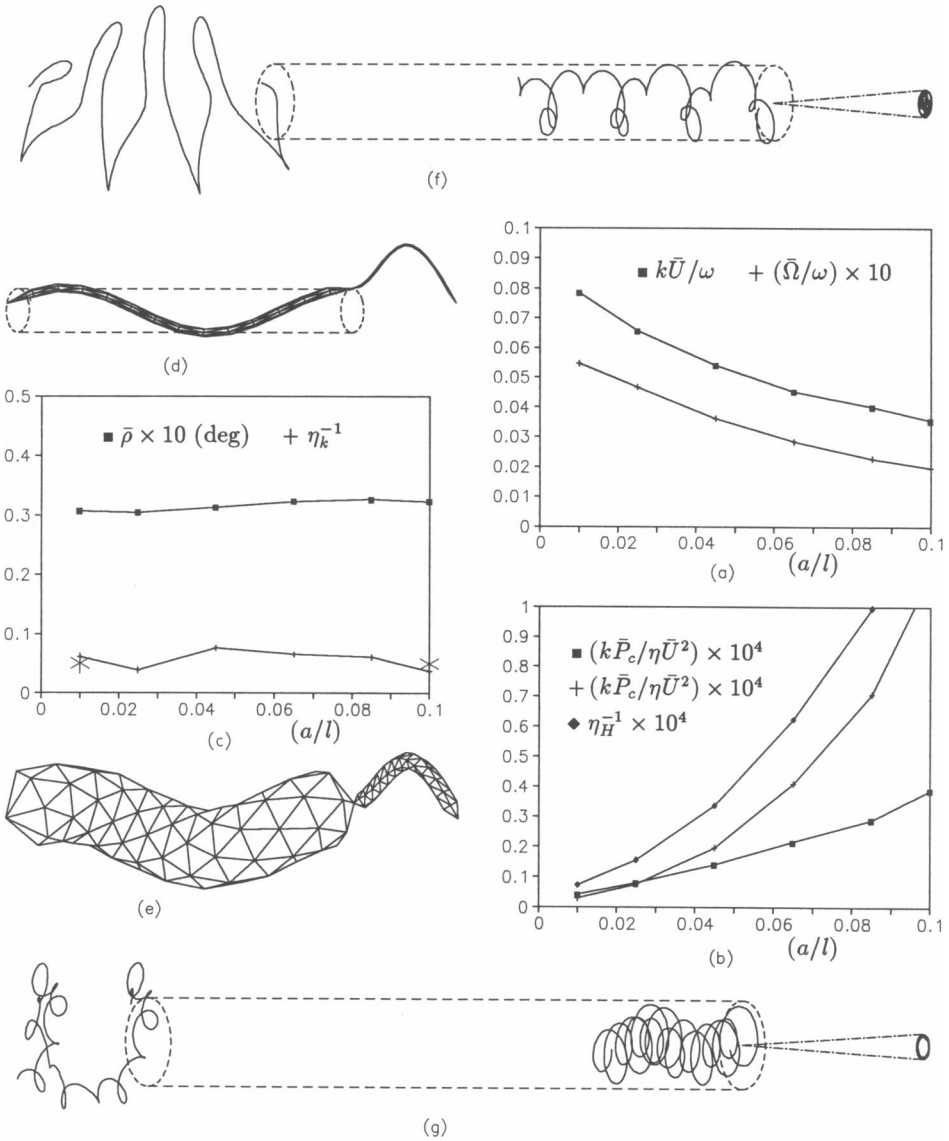

FIGURE 8 (*a–c*) Results as in Fig. 7 with the quantities plotted against the normalized cell-body radius (a/l). (*d–e* and *f–g*) Boundary element meshes and the corresponding trajectories for organisms with the parameter values (a/l) = 0.01 and (a/l) = 0.1 (shown as * on the graph of part *c*), respectively. The body cylinder defining the cell-body helix (viewed at 30° to the plane of the page) is also shown superposed on the mesh of part *d*. (Shown as * on the graph of part *c*.)

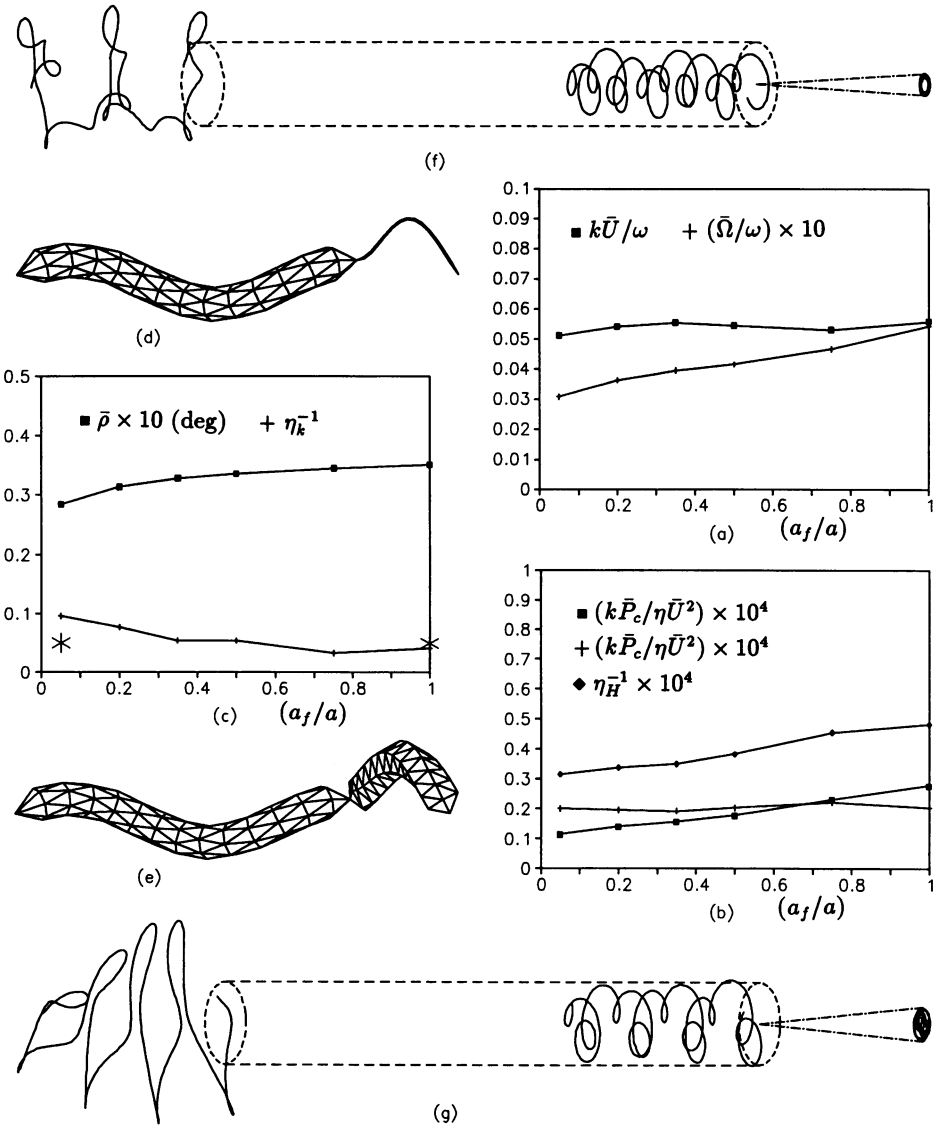

FIGURE 9 (*a–c*) Results as in Fig. 7 with the quantities plotted against the normalized flagellar radius a_f/a. (d–*e* and *f–g*) Boundary element meshes and the corresponding trajectories for organisms with the parameter values $(a_f/a) = 0.05$ and $(a_f/a) = 1$. (Shown as * on the graph of part *c*.)

normalized flagellar radius a_f/a. Here, there is an increase in the flagellar torque with a_f but due to the associated increase in flagellar resistance to counter rotation, only a slow increase in the mean angular velocity results. Initially, $k\overline{U}/\omega$ increases with $\overline{\Omega}/\omega$ in accordance with the corkscrew mechanism. But, this is progressively offset by the flagellar drag and the cell-body/flagellar hydrodynamic interaction, both being more prominent for thicker flagella.

The normalized cell body power $k\overline{P}_c/\eta\overline{U}^2$ increases with a_f/a whilst $\overline{\Omega}/\omega$ rises and the normalizing factor $\overline{U}$ remains essentially constant (see Fig. 9 *b*). The tendency for the increase in the flagellar power $k\overline{P}_f/\eta\overline{U}^2$, however, is negated by the reduction in the apparent (i.e., absolute) flagellar angular velocity $\boldsymbol{\Omega} + \boldsymbol{\omega}$ (with these angular velocities having opposite senses). Hence, the net effect is a slow but consistant increase in the total normalized power dissipation (i.e., η_H^{-1}).

Fig. 9 *c* shows that both the inverse kinematic efficiency η_k^{-1} and the precession angle $\bar{\rho}$ are effectively insensitive to variations in a_f/a. This and other results conveyed in this figure (Fig. 9) are analogous to those of Higdon (17) and Phan-Thien et al. (3), where it is reported that the swimming speed and hydrodynamic efficiency of a spher-

ically cell bodied microorganism are not heavily dependent on the flagellar radius.

Fig. 10 shows the results relating to variations in the normalized flagellar length l_f/l (where l is the cell body length). The flagellar amplitude α_f increases with its length l_f (compare Fig. 10 *d* to Fig. 10 *e*) and its torque increases with each of these independently. As a result, $\overline{\Omega}/\omega$ and consequently (due to the abovementioned corkscrew mechanism) $k\overline{U}/\omega$ rise rapidly throughout the considered range. For very low values of this parameter (i.e., <0.3) the absolute flagellar angular velocity $\mathbf{\Omega} + \boldsymbol{\omega}$ is close to $\boldsymbol{\omega}$ (because $\overline{\Omega}$ is close to zero) and the flagellum dissipates marginally more power than the essentially stagnant cell body. To a much lesser extent, the opposite is the case for very large flagella ($[l_f/l] > 0.6$), but the overall effect is a consistent decrease in total power dissipation (i.e.,η_H^{-1}). Hence, it would appear that the benefits represented by the steep rise in $\overline{U}$ and $\overline{\Omega}$ grossly outweigh the increase in the power consumption associated with the rotation of

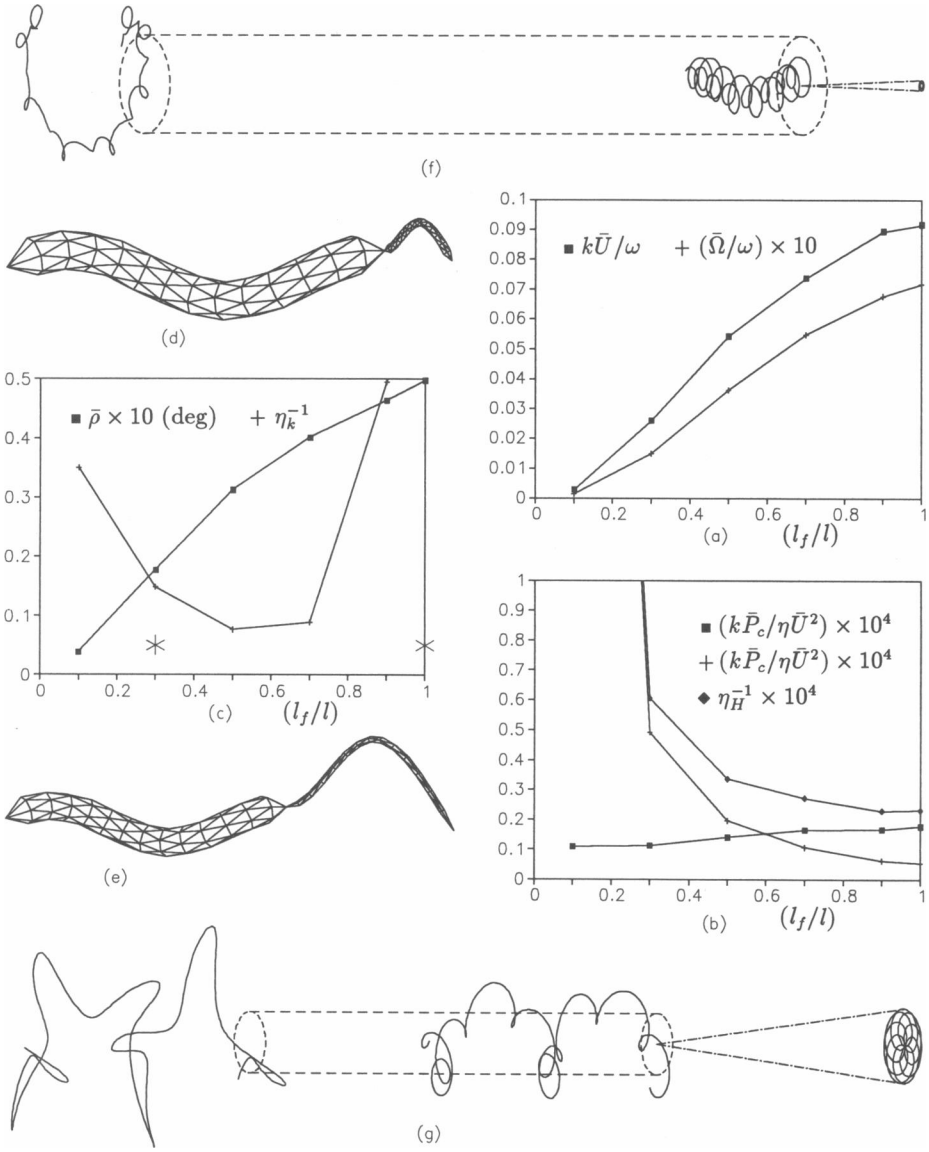

FIGURE 10 (*a–c*) Results as in Fig. 7 with the quantities plotted against the normalized flagellar length l_f/l. (*d–e* and *f–g*) Boundary element meshes and the corresponding trajectories for organisms with the parameter values $(l_f/l) = 0.3$ and $(l_f/l) = 1$ (shown as * on the graph of part *c*) respectively.

longer flagella. This is in agreement with the corresponding results of MS where a straight flagellar centerline geometry was employed. This implies that in examining the hydrodynamic swimming efficiency of *S. volutans* the flagellar length is a prominent consideration whilst its centerline geometry (for a given appropriately defined cone angle γ) is relatively insignificant. However, the hydrodynamically predicted optimum of $(l_f/l) = 1$ is unrealistically high because such long flagella would tend to assume a helical shape similar to those of the spherically cell bodied microorganism considered by Higdon (17) and Phan-Thien et al. (3).

Lower values of l_f/l lead to trajectories such as in Fig. 10*f* where the mean radial displacements are substantially smaller than the cell-body amplitudes, whilst for higher values the opposite is true (see Fig. 10*g*). Both these trajectories result in large values of inverse kinematic efficiencies η_k^{-1}. A kinematic optimum exists in the middle of the considered range near the typically realistic value $(l_f/l) = 0.5$, where η_k^{-1} is a minimum and the swimming motion best resembles that of the corkscrew mechanism.

Fig. 11 shows the results relating to variations in the normalized cell body wavenumber αk. Initially, the axisymmetric cell body of zero amplitude offers minimal resistance to rotation. As it grows in amplitude, the cell body then deviates from this symmetry and increases its resistance to rotation leading to a decrease in angular velocity. Here, the linear velocity increases steadily despite the decrease in angular velocity. This is primarily due to the consistent increase in the normalizing factor k being more prominent than the substantially slower decrease in $\overline{\Omega}$. For lower values of αk (i.e., <0.4), this is further enhanced by the extremely small cell body amplitudes rendering the corkscrew mechanism ineffective.

The inverse hydrodynamic efficiency decreases drastically from an originally large value (at $\alpha k = 0$) to its minimum near $\alpha k = 0.6$ reflecting the contrast between the initial nonexistence and sudden predominance of the corkscrew mechanism. This is further portrayed by the sharply defined minimum value of inverse kinematic efficiency η_k^{-1} near $\alpha k = 0.5$. With the growth of the amplitude α, the flagellum recedes from the cell body axis and the flagellar torque is progressively made to act further away from this axis resulting in a consistant increase in precession angle. This, together with the associated increase in the resistance to rotation of the cell body and to counter rotation of the flagellum lead to the steady increase in η_k^{-1} for $\alpha k > 0.6$. An extreme example of the combined effect of these factors may be seen in Fig. 11*g* where for some instants the precession angle is large enough to cause a backward movement of the leading point *B*. Hence, it is apparent that the kinematic optimum near $\alpha k = 0.5$ is in the same vicinity as its independently predicted hydrodynamic optimum, which lies well within the range of experimental observations of efficiently swimming spirilla.

In CWW an alternative definition of hydrodynamic efficiency was considered, namely P_c/P_t, to conclude that the axisymmetric case $\alpha k = 0$ is optimal. Based on this definition, their conclusion is also in agreement with that of the present study.

Fig. 12 shows the results relating to variations in the flagellar cone angle γ for unipolar trailing spirilla. An increase in γ (whilst the length l_f remains constant) results in a growing flagellar amplitude (see Fig. 3 and compare Fig. 12*d* to Fig. 12*e*). The flagellar torque and consequently $\overline{\Omega}/\omega$ increase consistently throughout the considered range. Initially, the swimming speed also increases (via the corkscrew mechanism) whilst the total normalized power decreases. However, these trends are eventually halted (in the vicinity of $\gamma = 55°$) and reversed by the flagellar contribution to drag becoming more prominent. It may be argued that this is due to the resistance to normal motion of a slender body being much larger than that to tangential motion. Namely, for larger γ the flagellum is subjected to a proportionately greater component of motion normal to its centerline.

The precession angle $\overline{\rho}$ increases slowly but consistantly with γ throughout the considered range. This trend is similar to those of Figs. 9*c* and 10*c* which may be rationalized to be a consequence of the increasing flagellar torque. The inverse kinematic efficiency has a minimum at $\gamma = 75°$ but, for this value $\overline{\rho}$ is quite large. Hence, there exists no clearly defined kinematic optimum for this parameter. On the other hand, a hydrodynamic optimum exists in the proximity of $\gamma = 55°$ where the independent conditions of maximum swimming speed and minimum normalized power (i.e., minimum η_H^{-1}) hold simultaneously.

5.2. Unipolar leading spirilla

Fig. 13 shows the results relating to variations in the flagellar cone angle γ for unipolar leading spirilla. The general trends for mean angular velocity, mean swimming speed, and normalized power dissipations are similar to those of trailing spirilla (shown in Fig. 12) with both the maximum velocity and minimum power occurring near $\gamma = 50°$. Here, however, cone angles $<30°$ may not be investigated as the flagellum will come into contact with the cell body at some part of its rotation cycle. Furthermore, for $\gamma < 60°$ both $k\overline{U}/\omega$ and $\overline{\Omega}/\omega$ are higher than those of the trailing case. This may be due to the amplitudes of leading flagella being greater than

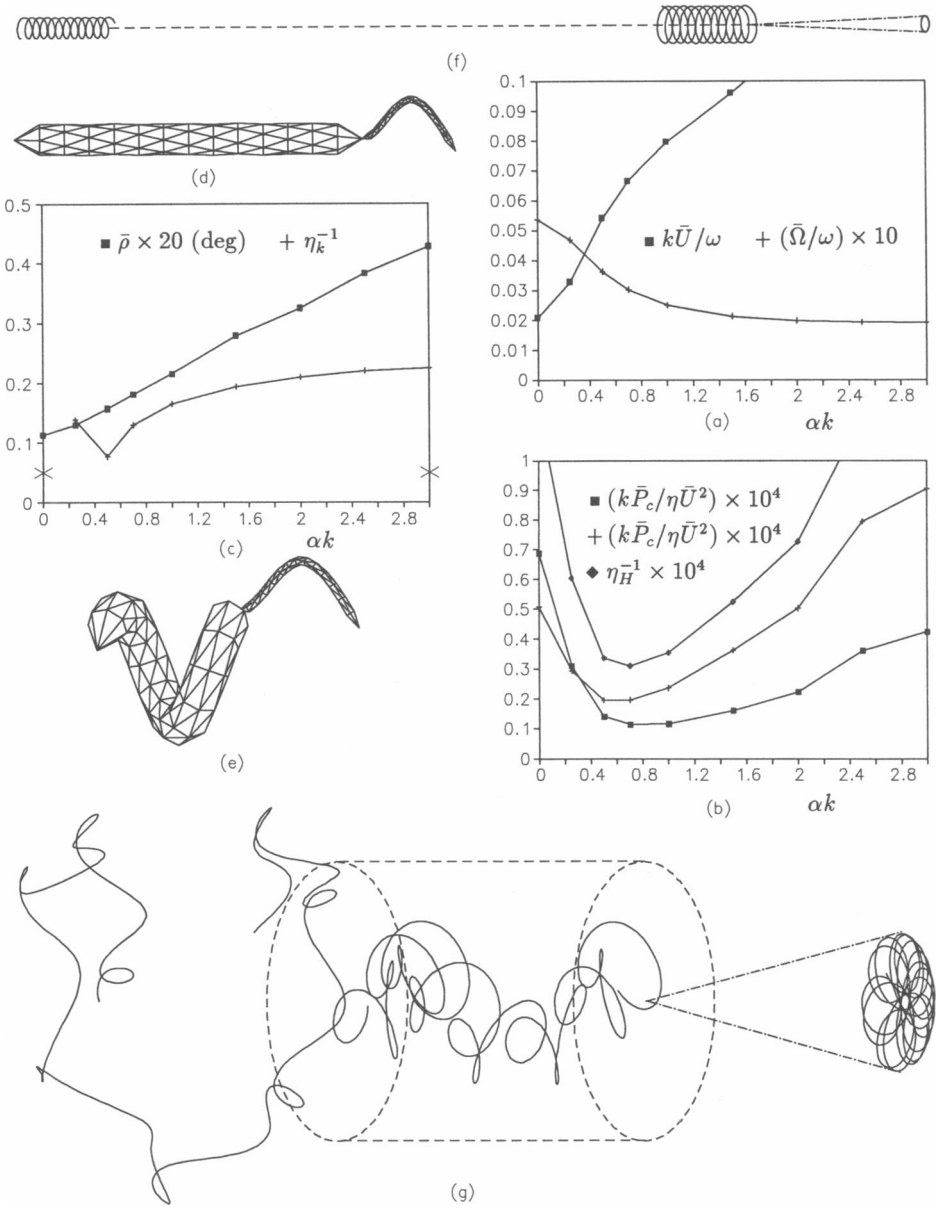

FIGURE 11 (*a–c*) Results as in Fig. 7 with the quantities plotted against the normalized cell-body wavenumber αk. (*d–e* and *f–g*) Boundary element meshes and the corresponding trajectories for organisms with the parameter values $\alpha k = 0$ and $\alpha k = 3$ (shown as * on the graph of part *c*), respectively.

those of trailing flagella (as illustrated in Fig. 3) whereby larger flagellar torques may be induced. The converse is true for $\gamma > 60°$ which contributes to a more severe drop in velocities and a steeper rise in inverse hydrodynamic efficiency.

Although a kinematic optimum is apparent at $\gamma = 60°$ both the precession angle and inverse kinematic efficiency vary negligibly with this parameter which is indicative of the stability of the leading flagellar configuration. This is further reflected by the slightly higher peak swimming speed of ~0.06 compared with that of 0.055 in Fig. 12.

The conclusions drawn from the results of Figs. 12 and 13 differ from those of MS where a hydrodynamic optimum near $\gamma = 90°$ is reported. This could only be accounted for by the differences in modeling the flagellar centerline geometry. From observations (4) it appears that upon reversing direction, the organism initially accelerates from rest with a flagellum which has a cone angle of almost 90° and a centerline geometry resem-

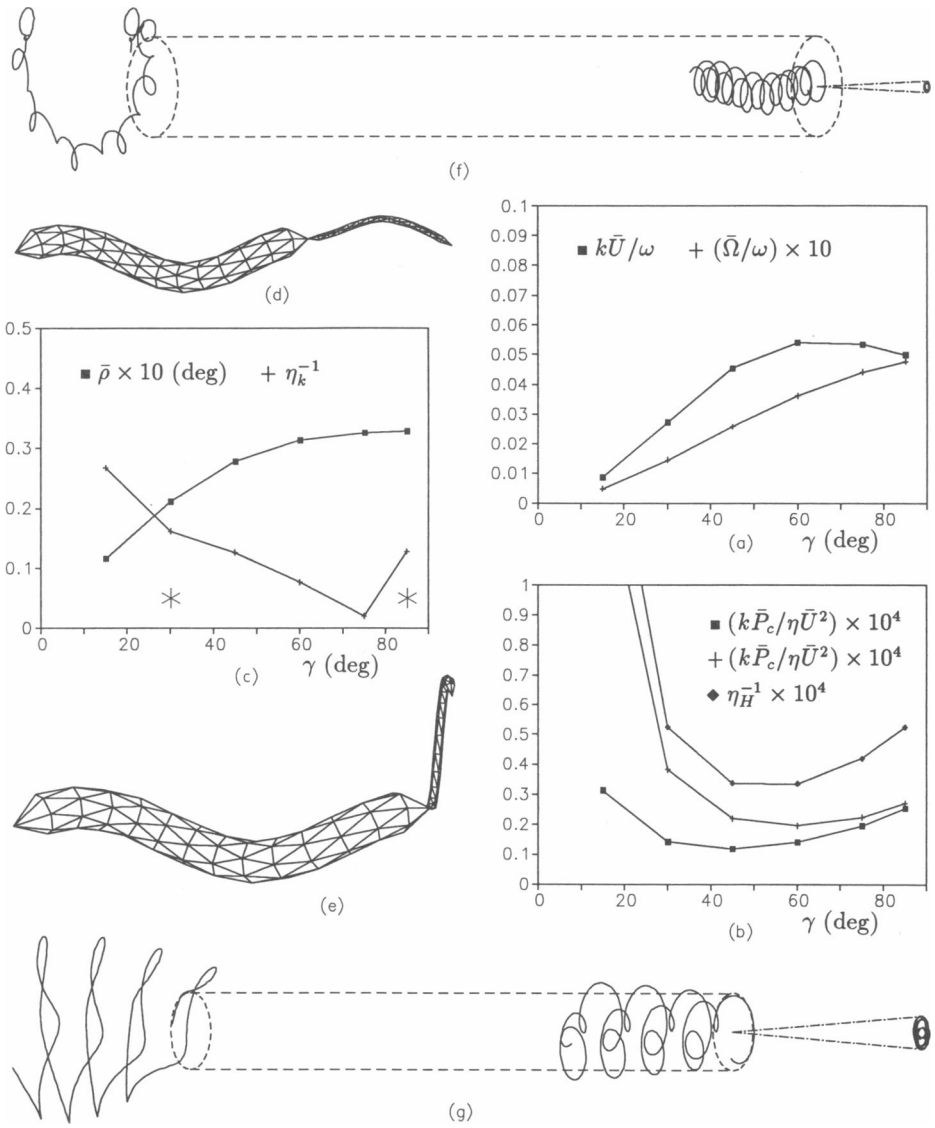

FIGURE 12 (*a–c*) Results as in Fig. 7 with the quantities plotted against the flagellar cone angle λ. (*d–e* and *f–g*) Boundary element meshes and the corresponding trajectories for organisms with the parameter values $\gamma = 30°$ and $\gamma = 85°$ (shown as * on the graph of part *c*), respectively.

bling that of a straight line. The viscous drag forces progressively bend the flagellum back in the axial direction and (with an opposite angular sense to its rotation) in the circumferential direction thereby reducing the cone angle and greatly distorting the flagellar geometry. Hence, whilst accelerating the flagellar centerline geometry is a function of time and the rotation frequency ω (which in turn varies with time). Under the equilibrium conditions of swimming with constant speed and constant angular velocity considered here, on the other hand, there exists a steady-state geometry of the flagellum and an associated constant cone angle of ~60° (see Fig. 3).

5.3. Bipolar spirilla

Fig. 14 shows the results relating to variations in the relative flagellar phase angle (i.e., the phase angle of the leading flagellum relative to the trailing flagellum) Δθ for a bipolar cell with $(l_f/l) = 0.3$, $N_\lambda = 2.0$, $(a/l) = 0.027$ and all other parameters as specified in Table 1. It is apparent that the angular velocity varies negligibly throughout the range considered. This reflects the minimal dependence of the combined torque of the two flagella on their relative orientation. The varying extent of flagellar/cell body hydrodynamic interaction leads to the appreciable variations in the mean swimming speed

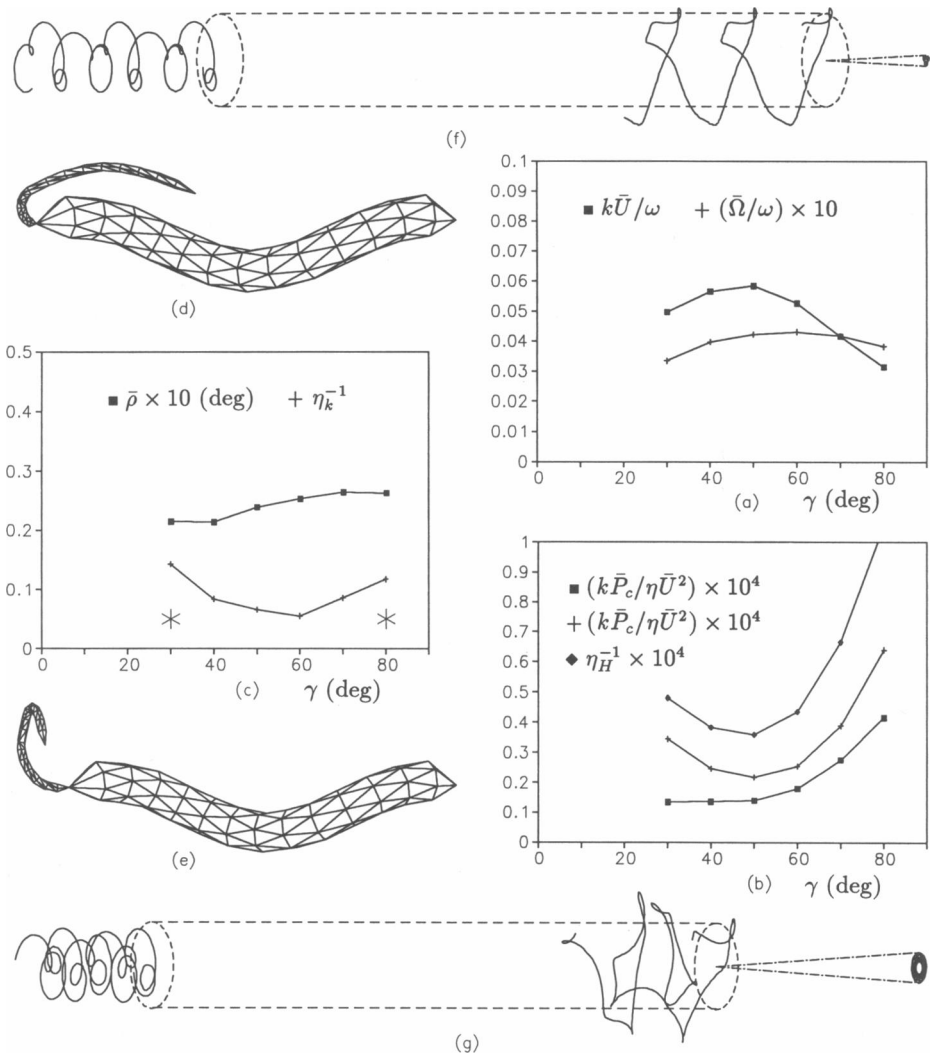

FIGURE 13 (*a–c*) As for Fig. 7, except relating to unipolar leading spirilla, with the quantities plotted against the flagellar cone angle γ. (*d–e* and *f–g*) Boundary element meshes and the corresponding trajectories for organisms with the parameter values $\gamma = 30°$ and $\gamma = 80°$ (shown as * on the graph of part *c*), respectively.

and normalized power dissipation components. The peak normalized swimming speed of nearly 0.08 for this organism with a substantially longer cell body (~70% longer than the unipolar cell) compares favorably to the corresponding velocity of the unipolar leading cell of ~0.06 (which in turn is slightly higher than that of the unipolar trailing cell). A clearly defined hydrodynamic optimum exists near $\Delta\theta = 90°$ where the velocity is a maximum and the total normalized power η_H^{-1} is a minimum.

The mean precession angle $\bar{\rho}$ is generally smaller than that of the corresponding unipolar cell. The implications of this may best be appreciated by noting that the trajectories of Figs. 14, *f* and *g* bear a much greater resemblance to the ideal corkscrew motion than those of the most kinematically efficient unipolar spirilla shown in Figs. 9*f* and 13*f*. An irregular spike appears in the inverse kinematic efficiency at $\Delta\theta = 135°$ which is associated with a complete and sudden change in the geometrical pattern of the trajectory. However, the effect of this change subsides when the mean quantity $\bar{\rho}$ is considered. Both ρ and η_k^{-1} are a minimum near $\Delta\theta = 0°$ describing the kinematically optimum condition of the two flagella rotating with the same phase angle. Hence, it may be concluded that to maintain $\Delta\theta$ at some appropriate optimum value and maintain a steady-state swimming trajectory (i.e., avoid any sudden changes such as those at $\Delta\theta = 135°$) both flagella must rotate

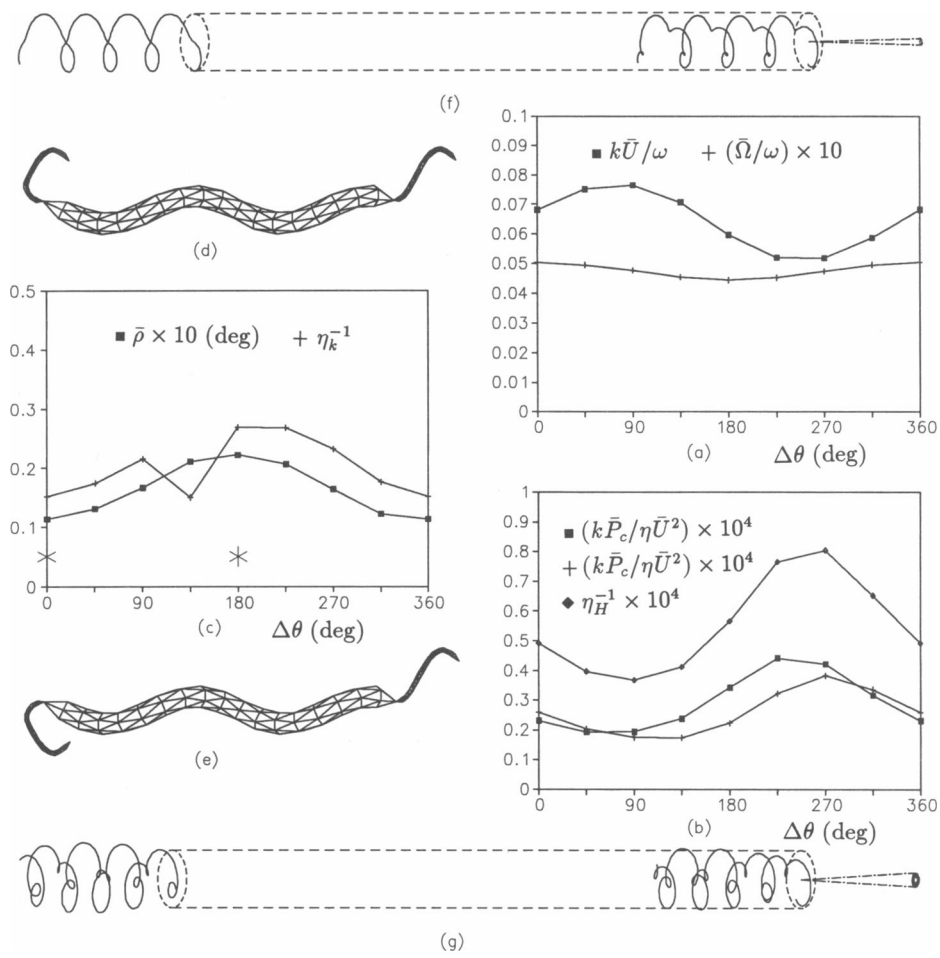

FIGURE 14 (*a–c*) Results as in Fig. 7 with the quantities plotted against the relative flagellar phase angle $\Delta\theta$ for bipolar spirilla. (*d–e* and *f–g*) Boundary element meshes and the corresponding trajectories for organisms with the parameter values $\Delta\theta = 0°$ and $\Delta\theta = 180°$ (shown as * on the graph of part *c*), respectively.

with the same angular frequency. This conclusion is in agreement with the observations of Winet and Keller (13).

5.4. Comparison with previous models and observations

A comparison of the present BEM predictions of the mean swimming speed and mean angular velocity with those of experimental observations, RFT of CWW and SBT of MS for the typically realistic unipolar trailing and leading cells (specified in Table 1) is as shown in Table 3.

Swan (4) observed each of 6 unipolar cells (of typical but varying dimensions) for at least 4 and up to 12 flagellar cycles whilst swimming in a trailing configuration. For each cell $k\overline{U}/\omega$ and $\overline{\Omega}/\omega$ were measured (and calculated) for a period representing an exact number of flagellar cycles. The same procedure was carried out on the same six cells whilst swimming in a leading configuration. The averages and standard deviations of the resulting normalized mean swimming speeds and normalized mean angular velocities are given in Table 3.

In addition to these results, MS illustrated the extent of pitching and yawing (i.e., precession) via tracings of such a cell at three instants separated by given constant time intervals (their Fig. 1). A direct comparison of this with the present predictions of precession angles is not feasible without knowledge of the flagellar rotation frequency ω and a greater, more representative, number of tracings per flagellar cycle.

The sinusoidal definition of the normalized mean swimming speed $k\overline{U}/\omega$ assumes the mean of the instantaneous velocities, for a given flagellar cycle, is aligned

TABLE 3 **Comparison of predicted mean swimming speeds with angular velocities (for a unipolar trailing Spirillum with the dimensions of table 1) with those of previous models and experimental observations.**

Unipolar trailing spirilla				
Values as predicted by the models or observed by experiment			Percentage error	
Quantity	$k\overline{U}/\omega$	$\overline{\Omega}/\omega$	$k\overline{U}/\omega$	$\overline{\Omega}/\omega$
RFT (CWW)	0.0933	0.2910	82.9	25.4
SBT (MS)	0.0279	0.1120	45.3	71.3
BEM (Sinusoidal mean def.)	0.1149	0.3616	125.3	7.6
BEM (Kinematic def.)	0.0540	—	5.8	—
Experimental observations (4)	0.051 ± 0.011	0.39 ± 0.16	—	—
Unipolar leading spirilla				
RFT (CWW)	0.0933	0.2910	117.0	51.5
SBT (MS)	0.0279	0.1120	35.1	81.3
BEM (Sinusoidal mean def.)	0.1618	0.4305	276.3	28.25
BEM (Kinematic def.)	0.0527	—	22.5	—
Experimental observations (4)	0.043 ± 0.019	0.60 ± 0.10	—	—

with the axis of the cell body. It was shown that this axis (which is always parallel to the z-axis) consistently defines a finite angle of precession with the axis of propagation (Z-axis) throughout the swimming motion. For this reason, the sinusoidal mean definition leads to gross over estimates of the mean swimming speed. Hence, it would appear that applying kinematics to the results of the SBT model of MS would serve to further magnify their discrepancy with experimental observations.

It is apparent that whilst both the RFT and the SBT models are based on simplified organism geometries, they do give a reasonable order of magnitude estimate of the experimentally observed mean swimming speed and angular velocity. The present BEM model yields a substantially better estimate of these quantities, but only when coupled with the relevant kinematic considerations.

6. CONCLUSION

In summary, it is concluded that the Boundary Element Method can successfully be applied to model the locomotion of spirilla and indeed of microorganisms generally. Unlike previous approaches such as Resistive Force Theory and Slender Body Theory, this method is not restricted to slender bodies, hence allowing the consideration of realistic organism geometries. However, averaging the BEM predicted instantaneous linear velocities throughout a given cycle proves to be insufficient as it leads to a consistently gross overestimate of the mean swimming speed. The necessary application of kinematics yields a substantially more realistic definition of this speed and a quantitative measure of pitching and yawing (i.e., precession).

Hydrodynamically, the optimum unipolar trailing organism must have a cell body with an amplitude and wavenumber such that $\alpha k = 0.6$. Its flagellum is to be of similar length to the cell body and rotate about the relevant axis to define a somewhat conical surface of revolution with an approximate half cone angle of 55°. Furthermore, both the cell body and flagellum must be as slender as possible. Although kinematic considerations lead to similar conclusions, they furnish the added constraints of $N_\lambda > 1$ and $l_f/l \approx 0.5$. This serves to correct the somewhat erroneous hydrodynamically deduced optima and validate the proposed ideal corkscrew mechanism.

Generally, the default values, which are based on typical estimates from cinemicrographs, vary negligibly from their corresponding numberically estimated optima. The only exceptions being the cell body and flagellar radii which may seemingly be subject to more prominent biophysical constraints.

7. APPENDIX 1

Each point on the surface of the cell body is considered to lie on the perimeter of a cross-sectional circle (centered about the centerline) of given constant radius (except very near the ends where the radius decreases sharply to zero). The length of the cell body is discretized into n_c segments, by considering a finite number of cross-sections, which are in turn discretized into polygons of v_c sides. These polygons are then used to model the entire cell-body surface by a series of (for example) hexagonal cylinders sealed at either end by a hexagonal pyramid. Each of the six quadrilateral faces of the cylinders (not necessarily flat) are further subdivided into two flat triangular boundary elements. Similarly, n_f segments and v_f sides are used in discretizing the flagellum (parts d and e of Figs. 7–14 show some resulting boundary element meshes). This results in N flat triangular boundary elements given by

$$N = 2[v_c(n_c - 1) + mv_f(n_f - 1)], \quad (25)$$

where m (the number of flagellar bundles) is assigned a value of 1 for unipolar spirilla and 2 for bipolar spirilla (see also Ramia and Tullock

TABLE A1 **Estimates of typical percentage errors in linear velocity, angular velocity, and power dissipation due to discretization**

Case and discretisation scheme	Case 1: $N = 616$ $v_c = 7, n_c = 14$ $v_f = 7, n_f = 32$	Case 2: $N = 616$ $v_c = 9, n_c = 28$ $v_f = 5, n_f = 14$	Case 3: $N = 618$ $v_c = 9, n_c = 20$ $v_f = 6, n_f = 24$	Case 4: $N = 618$ $v_c = 9, n_c = 20$ $v_f = 6, n_f = 24$
U_x	0.01	0.60	0.06	0.90
U_y	1.51	0.01	0.78	2.17
U_z	0.37	0.16	1.85	0.44
$\|\mathbf{U}\|$	0.93	0.39	0.15	0.36
Ω_x	0.36	0.04	0.19	0.09
Ω_y	0.00	0.23	0.10	0.21
Ω_z	1.89	0.02	0.60	0.18
$\|\mathbf{\Omega}\|$	1.87	1.55	0.60	0.19
P_t	2.23	3.14	3.43	5.20

[21] where a discretization of this organism into curved isoparametric quadratic elements is considered).

Throughout most of the calculations carried out in the present study, the following values were adopted:

$$v_c = 7, n_c = 14, v_f = 5 \quad \text{and} \quad n_f = 14 \quad \text{giving} \quad N = 312.$$

The only exceptions to these are unipolar trailing spirilla having in excess of 1.5 cell-body wavelengths (i.e., $N_\lambda > 1.5$ in Fig. 7) and bipolar spirilla (Fig. 14). In the former of these cases, n_c is gradually increased to 24 (see Fig. 7 *e* where $N_\lambda = 3$) to appropriately model the increased curvature of the cell-body centerline. For the latter case, however, a substantially different scheme is employed with:

$$v_c = 6, n_c = 18, v_f = 5 \quad \text{and} \quad n_f = 14 \quad \text{giving} \quad N = 464.$$

There are two major discretization errors. The first stems from the approximation of a continuously curved surface by a finite number of flat triangular faces. The second, however, results from the inaccuracy of the constant boundary elements of high aspect ratios (i.e., elements whose ratio of longest to shortest side is very large). Although both contribute to error in all cases, the former of these effects is most prominent for organisms with higher centerline curvature, and the latter for the more slender organisms. To quantify the typical errors involved, the instantaneously velocity **U**, angular velocity $\mathbf{\Omega}$, and total power dissipation P_t were recalculated in four different cases (having a zero flagellar phase angle) each with nearly twice the original number of elements. The resulting percentage errors, normalized with respect to $|\mathbf{U}|$, $|\mathbf{\Omega}|$, and P_t, respectively, are given in Table A1.

The most slender of the considered organisms is that depicted in Fig. 8 *d* where $a/l = 0.01$. This is considered in the first three cases of Table A1. In case 1, the extra boundary elements are utilized on the flagellum, in case 2, they are utilized on the cell body, whilst in case 3, they are evenly distributed throughout the entire organism. Amongst these three cases, the errors in both the instantaneous linear and angular velocities are consistently below 2%. The largest error in P_t, on the other hand, is nearly 3.5%. This is to be expected as both **U** and $\mathbf{\Omega}$ are determined from equilibrium considerations which primarily involve a surface integral of the traction (Eq. 12) and, P_t involves an integral (over the same surface) of the dot product of traction and velocity (Eq. 13). In the latter case, the intrinsic errors in both the traction and velocity contribute to the error in the resulting integral. In summary, these three cases illustrate that the errors introduced by slender boundary elements (aspect ratios of nearly 20) are acceptably small. This conclusion is also supported by the results of Phan-Thien et al. (3) which were based on similar discretizations.

In case 4 of Table A1, the typical organism with the default dimensions is considered. Here, the extra boundary elements are evenly distributed throughout the entire organism. Similar errors to those of the first three cases result for **U** and $\mathbf{\Omega}$, whilst a larger error results for P_t. But again, the errors are generally acceptably small.

Of more importance are the typical errors involved in the mean quantities considered in Figs. 7–14. These were determined for the default organism by considering the eight instants per flagellar cycles in case 4. The resulting errors are summarized here:

$k\overline{U}/\omega$	$\overline{\Omega}/\omega$	η_H^{-1}	η_k^{-1}	$\overline{\rho}$
1.03	0.14	6.60	0.27	1.20

With the exception of η_H^{-1} all of the above normalized quantities depend primarily on $\overline{U}_z$ and $\overline{\Omega}_z$ (see reference 15 for example, where the radial components $\overline{\Omega}_x$ and $\overline{\Omega}_y$ were assumed to be negligible compared with $\overline{\Omega}_z$), both involving errors smaller than 2%. Hence the relatively small errors in $k\overline{U}/\omega$, $\overline{\Omega}/\omega$, η_k^{-1}, and $\overline{\rho}$. The inverse hydrodynamic efficiency however (and other normalized power components) involves the power dissipation with which a substantially larger error is associated. The use of $\overline{U}^2$ as a normalizing factor is a further contribution to the error. Albeit, the plots of η_H^{-1} vs. the various geometrical parameters in Figs. 7–14 may safely be regarded as a qualitative indication of swimming efficiency.

The present study was made possible by the work of Dr. T. Tran-Cong who was responsible for the numerical implementation of the general boundary element method for locomotion and sedimentation problems (LOCOS). The author is indebted to Dr. N. Phan-Thein for many helpful comments and discussions and Dr. J. D. Atkinson for his help with numerical methods and the Fortran programming language.

This research is partly funded by the Australian Research Grants Scheme (ARGS).

Received for publication 5 November 1990 and in final form 19 March 1991.

REFERENCES

1. Chwang, A. T. and T. Y. Wu. 1971. A note on the helical movement of micro-organisms. *Proc. R. Soc. Lond. B. Biol. Sci.* 178:327–346.

2. Higdon, J. J. L. 1979*a*. A hydrodynamic analysis of flagellar propulsion. *J. Fluid Mech.* 90:685–711.
3. Phan-Thien, N., T. Tran-Cong, and M. Ramia. 1987. A boundary-element analysis of flagellar propulsion. *J. Fluid Mech.* 184:533–549.
4. Swan, M. A. 1982. Trailing flagella rotate faster than leading flagella in unipolar cells of Spirillum volutans. *J. Bacteriol.* 150:377–380.
5. Anderson, R. A. 1975. Formation of the bacterial flagellar bundle *In* Swimming & Flying in Nature. T. Y. Wu, C. J. Brokaw, and C. Brennen, editors. New York, Plenum. 1:45–56.
6. Chwang, A. T., H. Winet, and T. Y. Wu. 1972. Locomotion of spirilla. *Biophys. J.* 12:1549–1561.
7. Gray, J., and G. J. Hancock. 1955. The propulsion of sea-urchin spermatozoa. *J. Exp. Biol.* 32:802–814.
8. Lighthill, M. J. 1976. Flagellar hydrodynamics: the John von Neuman lecture. *SIAM Rev.* 18:161–229.
9. Myerscough, M. R., and M. A. Swan. 1989. A model for swimming unipolar spirilla. *J. Theor. Biol.* 139:201–218.
10. Hancock, G. J. 1953. The self propulsion of microscopic organisms through liquids. *Proc. R. Soc. Lond. A.* 217:96–121.
11. Cox, R. G. 1970. The motion of long slender bodies in a viscous fluid. *J. Fluid Mech.* 44:791–810.
12. Johnson, R. E. 1980. An improved slender body theory for Stokes flow. *J. Fluid Mech.* 99:411–431.
13. Winet, H., and S. R. Keller. 1976. Spirillum swimming: theory and observation of propulsion by the flagellar bundle. *J. Exp. Biol.* 65:577–602.
14. Swan, M. A. 1985. Electron microscopic observations of structures associated with the flagella of Spirillum volutans. *J. Bacteriol.* 161:1137–1145.
15. Keller, J. B., and S. I. Rubinow. 1976. Swimming of flagellated micro-organisms. *Biophys. J.* 16:151–170.
16. Tran-Cong, T., and N. Phan-Thien. 1986. Boundary element solution for half-space elasticity or Stokes problems with a no-slip boundary. *Comp. Mech.* 1:259–268.
17. Higdon, J. J. L. 1979*b*. The hydrodynamics of flagellar propulsion: helical waves. *J. Fluid Mech.* 94:331–351.
18. Ramia, M., and N. Phan-Thien. 1988. The motion of slender bodies in a viscous fluid: a boundary element approach. *Proc. Xth internat. Congr. Rheol., Sydney, Aug. 14–19.* P. H. T. Uhlherr, editor. 2:193–195.
19. Banerjee, P. K., and R. Butterfield. 1981. Boundary Element Methods in Engineering Science. McGraw-Hill, New York. 138–167.
20. Brebbia, C. A., C. F. Telles and L. C. Wrobel. 1984. Boundary Element Techniques: Theory and Application in Engineering. Springer Verlag, Berlin. 177–236.
21. Ramia, M., and D. Tullock. 1988. Microorganism locomotion: an application of fluid mechanics and kinematics. *Proc. Vth Nat. Conf. Rheol., 1990, Melbourne, June 27–29.* Y. L. Yeow and P. H. T. Uhlherr, editors. 95–98.
22. Goldstein, H. 1950. Classical Mechanics. Addison-Wesley Publishing Co. Ltd., London. 93–143.
23. Gray, J. 1968. Animal Locomotion. W. W. Norton & Co., Inc., New York.